The Astrophysical Journal, 741:115 (20pp), 2011 November 10 doi:10.1088/0004-637X/741/2/115

THE ASSEMBLY HISTORY OF DISK GALAXIES. I. THE TULLY–FISHER RELATION TO $z \simeq 1.3$ FROM DEEP EXPOSURES WITH DEIMOS

Sarah H. Miller[1,2], Kevin Bundy[3], Mark Sullivan[1], Richard S. Ellis[2], and Tommaso Treu[4]
[1] Oxford Astrophysics, Oxford, OX1 3RH, UK; s.miller1@physics.ox.ac.uk
[2] California Institute of Technology, Pasadena, CA 91125, USA
[3] Astronomy Department, University of California, Berkeley, CA 94720, USA
[4] UC Santa Barbara Physics, Santa Barbara, CA 93106, USA
Received 2011 February 18; accepted 2011 August 15; published 2011 October 25

ABSTRACT

We present new measures of the evolving scaling relations between stellar mass, luminosity and rotational velocity for a morphologically inclusive sample of 129 disk-like galaxies with $z_{AB} < 22.5$ in the redshift range $0.2 < z < 1.3$, based on spectra from DEep Imaging Multi-Object Spectrograph on the Keck II telescope, multi-color *Hubble Space Telescope* (*HST*) Advanced Camera for Surveys photometry, and ground-based K_s-band imaging. A unique feature of our survey is the extended spectroscopic integration times, leading to significant improvements in determining characteristic rotational velocities for each galaxy. Rotation curves are reliably traced to the radius where they begin to flatten for ∼90% of our sample, and we model the *HST*-resolved bulge and disk components in order to accurately de-project our measured velocities, accounting for seeing and dispersion. We demonstrate the merit of these advances by recovering an intrinsic scatter on the stellar mass Tully–Fisher relation a factor of two to three less than in previous studies at intermediate redshift and comparable to that of locally determined relations. With our increased precision, we find that the relation is well established by $\langle z \rangle \sim 1$, with no significant evolution to $\langle z \rangle \sim 0.3$, $\Delta M_* \sim 0.04 \pm 0.07$ dex. A clearer trend of evolution is seen in the *B*-band Tully–Fisher relation corresponding to a decline in luminosity of $\Delta M_B \sim 0.85 \pm 0.28$ magnitudes at fixed velocity over the same redshift range, reflecting the changes in star formation over this period. As an illustration of the opportunities possible when gas masses are available for a sample such as ours, we show how our dynamical and stellar mass data can be used to evaluate the likely contributions of baryons and dark matter to the assembly history of spiral galaxies.

Key words: galaxies: evolution – galaxies: fundamental parameters – galaxies: kinematics and dynamics – galaxies: spiral

Online-only material: color figure, machine-readable table

1. INTRODUCTION

A major challenge for ΛCDM structure formation lies in understanding how the baryonic components of galaxies assemble within dark matter halos. Although baryons represent only one-sixth of the gravitating matter in *Wilkinson Microwave Anisotropy Probe* cosmology (Spergel et al. 2007; Seljak et al. 2005), their dissipative properties suggest that they dominate the inner regions of luminous galaxies (Blumenthal et al. 1986). Determining the interplay between dark matter and baryons is critical for predicting the evolution of density profiles, substructure, shapes, and angular momentum of galaxies (Governato et al. 2007; Shlosman 2009). One of the most significant challenges is reproducing the detailed characteristics of rotationally supported disk galaxies which represent the dominant fraction of present-day luminous systems (Ellis & Silk 2009).

Observational efforts in this challenge have focused on the Tully–Fisher (TF) relation (Tully & Fisher 1977) and its past evolution. This important scaling relation, which correlates disk luminosity with rotational velocity, provides an essential benchmark for verifying theoretical models based on the standard dark matter picture. Early *N*-body simulations as well as semi-analytic models produced galaxies that rotate too fast at a given luminosity (van den Bosch 2000; Mo & Mao 2000; Eke et al. 2001; Benson et al. 2003; Dutton et al. 2007). Caused by a transfer of angular momentum from baryons to the dark matter halo, this deficiency has since been mitigated by improved resolution, as well as the introduction of feedback (Steinmetz & Navarro 1999), e.g., from supernovae (Governato et al. 2007; Piontek & Steinmetz 2011). However reproducing the absolute values observed in the scaling relation has remained problematic.

Despite these challenges, the theoretical understanding of disk galaxy scaling relations and their evolution has made some improvement over the past decades. Using an adjustment to the rotational velocity derived from their hydrodynamic simulations to account for overmerging, Portinari & Sommer-Larsen (2007) were able to match the observed local TF relation, and claim a modest evolution to $z \sim 1$. However the predictive power is tempered by an unknown dependence on redshift of this adjustment. Semi-analytic models have also worked to match observations and provide further insight on the physical interpretation of evolution in the TF relation. Some controversy remains over whether the central regions of galaxy halos are subject to adiabatic contraction (Somerville et al. 2008), broadly maintain a non-evolving density profile (Wechsler et al. 2002), or permit adiabatic expansion (Dutton et al. 2011c). Regardless of the exact evolutionary response of the inner halo, the persistent picture is one in which the baryonic component grows in tandem with the dynamical mass (Fall & Efstathiou 1980; Dalcanton et al. 1997; Mo et al. 1998). Gas may cool from the halo or from externally sourced streams, increasing the disk scale length as stars form. In this framework, while any given galaxy is predicted to grow by factors of 1.2–2 in stellar mass, dynamical mass, scale radius, and luminosity since $z \sim 1$ (modulo evolutionary corrections), this growth typically occurs *along* scaling relations, reducing the evolutionary signals accessible to observations.

Observational progress in testing these pictures of disk assembly has been similarly slow. There are significant technical challenges in making the necessary measurements at intermediate redshift and, as a result, there are discrepant conclusions with regard to evolutionary trends in the literature. In part, this may reflect different ways in which intermediate-redshift disk galaxies are selected. Vogt et al. (1996, 1997) undertook an important pioneering study, finding a modest increase in luminosity ($\Delta M_B \sim 0.6$) at fixed velocity to $z \sim 1$, but deduced this represented only an upper limit to possible evolution because of sample biases and other assumptions. Subsequent optical-based studies have presented mixed conclusions. A key uncertainty is whether to address evolution in the overall mass-to-light ratio independent of luminosity (i.e., a zero-point shift with redshift) as discussed by Rix et al. (1997), Bamford et al. (2006), and Fernández Lorenzo et al. (2009, 2010), or whether to permit luminosity dependent evolution (i.e., changes in the TF slope) as discussed by Ziegler et al. (2002) and Böhm et al. (2004). TF studies at infrared wavelengths are less affected by biases induced by short-term star formation activity and early surveys found no convincing evolution (Conselice et al. 2005; Flores et al. 2006). However, by contrast, Puech et al. (2008) claim from near-IR measures that disks were overall *less luminous* in the past. Clearly the rest wavelength at which the luminosity is sampled is a key parameter: Fernández Lorenzo et al. (2010) claim evolution in the *B*-band but none in redder bands, while Weiner et al. (2006a, 2006b) find evolution in the slope of the infrared TF relation consistent with that seen in the blue relation; however, they observe little evolution in infrared zero point. Moran et al. (2007) have emphasized the importance of environmental influences which can be deduced by considering the scatter in the TF relation as a function of local density.

In view of this, a more physically relevant approach for understanding the assembly history of disks may be to consider the *stellar mass TF relation* (M_*-TF) which, notwithstanding the difficulty of estimating gas fractions, provides the most robust route to understanding the interplay between baryons and dark matter in disk galaxies. Stellar masses are derived using population model fits to multi-color photometry for galaxies of known redshift, assuming an initial stellar mass function (Brinchmann & Ellis 2000; Bundy et al. 2005). Although the low-redshift M_*-TF relation is well constrained (Bell & de Jong 2001; Pizagno et al. 2005; Meyer et al. 2008), those at intermediate redshift (Conselice et al. 2005; Flores et al. 2006; Atkinson et al. 2007) reveal a larger scatter than seen in the traditional TF relations, suggestive of additional uncertainties. A recurrent topic of discussion in the literature is sample selection and whether evolution seen in both the TF relation and its scatter is driven by redshift-dependent selection criteria. The inclusion of more early types and dynamically disturbed galaxies likely broadens the intrinsic scatter. In an attempt to include more kinematically disturbed galaxies, often excluded without good cause in TF studies, Weiner et al. (2006b) and Kassin et al. (2007) have included an additional kinematic term, $S_{0.5}$, which accommodates the isotropic velocity width of the observed emission lines and reduces the scatter from their classic M_*–rotational-velocity relation. Kassin et al. (2007) detect no significant evolution in the TF relation, including the $S_{0.5}$ relation, over $0.1 < z < 1.2$. However, combining a measure of the velocity dispersion with the disk angular momentum may obscure information about the rotational support of the disk.

Using integral field unit (IFU) spectrographs, Flores et al. (2006) and Puech et al. (2008) have produced intensity, velocity, and dispersion maps of galaxies at intermediate redshifts that demonstrate the unique advantage of a second spatial dimension in modeling the velocity field and accounting for projection effects. So far, the IFU-based samples are fairly modest in size and sample brighter sources compared to those reached with multi-slit techniques. Moreover, the spaxel resolution is often lower than for the highest-resolution slit spectroscopy. As we will show in this paper, the spectroscopic S/N is an equally important factor in making progress because it determines the radial extent to which emission lines can be traced and as a result, whether the adopted velocity measure requires extrapolation.

Both IFUs and slit spectroscopy have been successfully employed at $z \approx 2$–3, where near-IR studies can take advantage of redshifted Hα lines—the brightest kinematic tracer—as well as improved spatial resolution from adaptive optics. Results at these redshifts may indicate the emergence of regular scaling relations from more complex and disordered dynamical states. With adequate sampling, at least one-third of $z \simeq 2$–3 star-forming galaxies show ordered rotation (Shapiro et al. 2008; Stark et al. 2008; Jones et al. 2010) and reveal significantly higher velocity dispersions than local counterparts (e.g., Genzel et al. 2006). Cresci et al. (2009) have measured the M_*-TF relation at $z \approx 2$ using Spectrograph for INtegral Field Observations in the Near-Infrared (SINFONI) observations of 18 rotation-dominated systems in the SINS survey (Spectrograph Imaging Survey in the Near infrared with SINFONI; Förster Schreiber et al. 2009). The slope of their measured relation is consistent with that seen in local observations but offset toward lower M_* at fixed velocity by $\sim$0.5 dex. While necessarily biased toward massive systems with well-ordered rotation, these may be representative of gas rich systems in transition to $z \sim 1$ disks (Tacconi et al. 2010). Gnerucci et al. (2011) have recently measured the TF relation at $z \sim 3$ from SINFONI IFU data, but because of the large scatter observed, they suggest the TF relation has not yet been established. However, all points on the relation are consistent with the favored vector of disk assembly theory, with a lower average stellar-to-dynamical mass ratio than found in the local universe.

The present survey was motivated by our desire to chart and understand this evolution from a prevalence of disturbed and complex dynamical states observed at high z to the well-ordered rotation of local spirals. To make progress, we seek to determine the M_*-TF relation over the redshift range $0.2 < z < 1.3$ with spectroscopic exposures three to eight times that of previous studies. By including disk systems selected from *Hubble Space Telescope* Advanced Camera for Surveys (*HST*/ACS) data with irregular or distorted morphologies, we hope to avoid biases based on selecting mature, well-ordered disks (Vogt et al. 1996, 1997). Our study not only allows us to chart evolution in a large sample down to fainter limits and masses than is possible at $z \sim 2$, but the improved precision we demonstrate enables us to measure a robust TF relation only a few Gyr later. The scatter we observe should provide a valuable indication of the rate at which disks settle onto the local TF relation. To fully utilize the gains in S/N ratio from long exposures, we develop an improved method for extracting the rotation curves of galaxies at intermediate redshift via a new modeling code. While our results are based on slit spectroscopy, unlike most previous slit-based studies (Weiner et al. 2006a; Kassin et al. 2007; Böhm & Ziegler 2007), we are able to align the spectral slits on our masks with the *HST*-measured major axis, significantly improving the fidelity of our recovered rotation curves at $z \sim 1$. We aim to

avoid introducing a bias toward aligning the often more extended and brighter objects at lower redshift over the higher redshift objects observed at smaller angular scales, since doing so could introduce an extraneous evolution in the offset and scatter of the TF relation with redshift.

The plan of the paper follows. In Section 2, we describe our sample, the Keck spectroscopic data, and the *HST*/ACS resolved photometry in the north and south Great Observatories Origins Deep Survey (GOODS) fields. Noting the limitations of earlier work, Section 3 introduces a new procedure for the analysis of rotation curve data. We justify our chosen method, discuss error estimation, and compare with previous work. In Section 4 we present the various TF relations, and in Section 5 we discuss methods for deriving dynamical masses to compare to baryonic mass estimates for a physical interpretation of our results. Finally, Section 6 summarizes the overall conclusions for the assembly history of disk galaxies.

Throughout the paper we adopt a Chabrier (2003) initial mass function (IMF) and a $\Omega_\Lambda = 0.7$, $\Omega_m = 0.3$, $H_0 = 70$ km s^{-1} Mpc^{-1} cosmology. All magnitudes refer to those in the AB system.

2. DATA

A prerequisite for constructing a disk galaxy sample suitable for measuring the evolution of the TF relation is deep *HST* imaging essential for morphological selection, resolved photometry and accurate disk position angle data for the multi-slit spectroscopic campaign. Both northern and southern GOODS fields (Dickinson et al. 2003) are visible from the Keck observatory and remain the most appropriate areas for such a study given the unique availability of deep multi-color ACS data. In this section we introduce our sample selection criteria (Section 2.1) and the spectroscopic data used for measuring the internal dynamics of our sample (Section 2.2). We also introduce the photometric data used for measuring galaxy sizes and shapes (Section 2.3) and stellar mass estimates from spectral energy distribution (SED) fitting (Section 2.4).

2.1. Sample Selection

Our goal in the morphological selection of disk targets is to be inclusive of all galaxies with disk-like structure, avoiding the temptation of selecting the most relaxed and "well-behaved" spirals in favor of a more complete census, including the more disturbed and morphologically abnormal population. Sources were selected visually by coauthor R.S.E. from a $z_{F850LP} < 22.5$ sample of 2978 galaxies, in the GOODS North and South fields, discussed by Bundy et al. (2005). A key difference with earlier work (i.e., Vogt et al. 1996, 1997; Conselice et al. 2005) is the inclusion of less mature morphological types which contain some evidence of disk-like structure, as well as systems that may be interacting. We included visually irregular systems with elongated features, and galaxies with asymmetric and clumpy light distributions. We also included disks with dominant bulges. The main aim of broadening the morphological selection criteria was to avoid potential biases associated with selecting only symmetric spirals, which may represent the end point of evolution and consequently bias us to locating mature systems. Within this z-band limited sample, we applied a further photometric selection, $K_s \leqslant 22.2$, to ensure a high fraction of reliable stellar mass (M_*) estimates to (see Section 2.4), resulting in a morphologically suitable sample of 1388 objects. Although spectroscopic redshifts are available for many of our targets from the Team Keck Redshift Survey program (TKRS; Wirth et al. 2004) in GOODS-N and from the VIMOS-VLT Deep Survey (Le Fèvre et al. 2004) in GOODS-S, we did not exclude targets for which only photometric redshifts were available. Selecting within our target redshift range of $0.2 < z < 1.3$, we used photometric redshifts from COMBO17 (Wolf et al. 2004) and Bundy et al. (2005). As discussed later (Section 3.5), several galaxies within our sample can be found in earlier kinematic surveys of Flores et al. (2006) and Weiner et al. (2006a).

2.2. Spectroscopic Data

Over a number of seasons we collected spectroscopic data for this sample with the DEIMOS (DEep Imaging Multi-Object Spectrograph; Faber et al. 2003) instrument on Keck II. In total, we examined 236 galaxies drawn from the target list discussed in Section 2.1 (17% of total sample), simply chosen to maximize number of objects with best position angle alignment with that of the mask. Of the 236 spectra, 129 show line emission extending past what we will term the "seeing-dispersion beam,"[5] 59 have only very compact emission lines that sample the central region, and 48 are in a category we will refer to as "passive" (meaning galaxies which show no significant emission lines across the two-dimensional (2D) spectrum, although weak lines may be recovered in the integrated spectrum; Figure 1 and Table 1).

The bulk of our analysis is thus based on the 129 galaxies with extended line emission. While this subsample makes up only 55% of our initially targeted sample, there is no statistical difference in its redshift or apparent magnitude distribution from the compact and passive subsets (Figure 1). The only obvious differences among the three subsamples concerns their disk sizes and stellar masses. Disks with extended line emission have larger scale radii than those of the compact and passive subsamples, and passive galaxies are largely drawn from the upper end of the total stellar mass distribution (see Table 1). These differences are not surprising and do not lead us to suspect that our working sample of 129 disk galaxies is significantly biased in its range of physical properties compared to the original parent selection. We discuss the properties of our compact emission line sources in a later paper in this series.

The DEIMOS observations were undertaken over a series of runs from 2004 March through 2008 April. Slit masks were designed with position angles (P.A.s) within $\pm 30^\circ$ of the measured P.A. in order to minimize tilt angle corrections in the reduction process. We used the 1200 l mm^{-1} grating blazed at 7500 Å with 1″ slits (with exception of 7 galaxies observed with the 600 l mm^{-1} grating blazed at 7500 Å). In this configuration, we achieved a spectral resolution of 1.7 Å corresponding to a velocity accuracy of 30 km s^{-1}. All DEIMOS data were reduced using the automated spec2d pipeline[6] developed by the DEEP2 survey. The spec1d package[7] (Davis et al. 2003) was used to extract one-dimensional (1D) spectra from the rectified 2D spectra produced by spec2d. The combination of 1D and 2D spectra were analyzed using the zspec software, also developed by DEEP2 (Faber et al. 2007; Coil et al. 2004), which fits a linear combination of galaxy, emission line, and stellar template spectra to each spectrum and allows the user to select the best-fitting template, thus determining the spectroscopic redshift.

[5] The seeing-dispersion beam signifies a 2D Gaussian representing the combination of the effect of seeing along the spatial axis and the emission line velocity dispersion along the wavelength axis.

[6] http://astro.berkeley.edu/~cooper/deep/spec2d/

[7] Based on http://spectro.princeton.edu/idlspec2d_install.html.

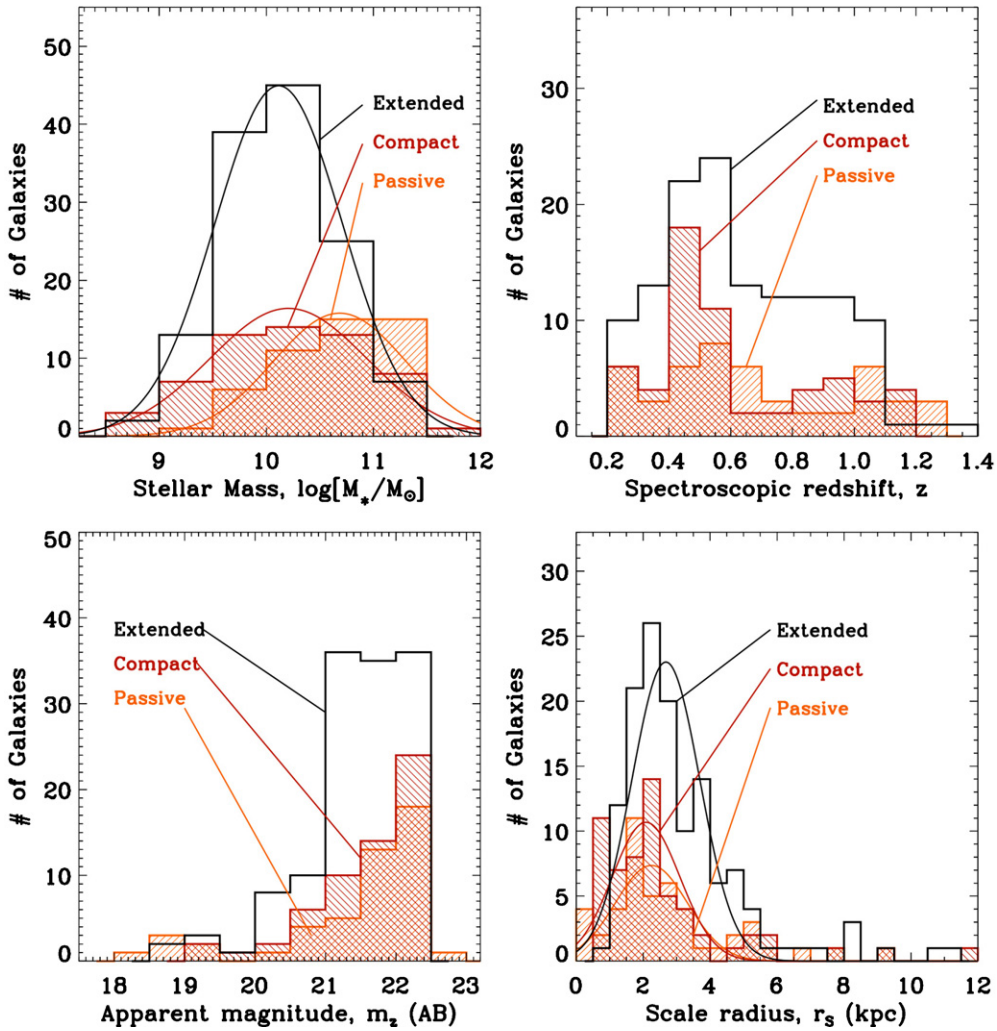

Figure 1. Properties of galaxies in our sample in terms of the distributions of stellar mass estimates, spectroscopic redshifts, z_{F850LP} apparent magnitudes, and disk scale radii. Each histogram is partitioned according to galaxies which have extended emission lines (129), passive spectra with no emission (49) and spectrally compact sources where emission does not extend beyond the central-most regions of their disks (59) (see Section 2.2 and Table 1 for details).

(A color version of this figure is available in the online journal.)

Table 1
Disk Sample

Line Profile	N	$\langle \log M_* \rangle$[a]	σ_{M_*}[b]	$\langle r_s \rangle$[c]	σ_{r_s}[d]
Extended[e]	129	10.11 ± 0.05	0.60	2.68 ± 0.09	1.02
Compact	59	10.21 ± 0.10	0.73	2.09 ± 0.13	1.01
Passive	48	10.69 ± 0.09	0.62	2.24 ± 0.16	1.08
Total	236				

Notes. See Figure 1 for histogram and best Gaussian fits of stellar mass and scale radii distribution.

[a] Best-fit Gaussian centroid of log stellar mass.

[b] FWHM of best-fit Gaussian of log stellar mass.

[c] Best-fit Gaussian centroid of scale radii in kpc.

[d] FWHM of best-fit Gaussian of scale radii in kpc.

[e] Possible to fit rotation curves.

This redshift was used as the initial guess for the systematic velocity in our rotation curve models discussed below.

Because we are interested in the 2D segments of specific emission lines in the spectra, particular care was taken to separate the reductions of a given mask observed at different hour angles (and therefore different parallactic angles), taken on different runs, or observed under varying conditions. A scheme (discussed below) was developed to coadd 2D spectra of the same target from multiple observation sets prior to further analysis. Because the spatial position of an emission line can vary from one observation to the next as a function of wavelength (by $\sim 0\farcs2$), we choose to extract $\approx$100 Å wavelength "cutouts" around key emission lines of interest (the [O II] 3727 Å doublet, Hβ, the [O III] 4959, 5007 Å doublet and Hα) for our rotation curve study, based on the redshift determined by the ZSPEC analysis.

Given a set of cutouts for the observation sets of a particular galaxy and emission line, we constructed optimally weighted coadditions, with weights based on the signal-to-noise ratio (S/N) and seeing FWHM measured from alignment stars on the corresponding slit masks. Typically five to six alignment stars were included on each mask. Relatively sky-free windows (with $\Delta\lambda \lesssim 500$ Å) were selected on both the blue and red sides of each alignment star spectrum. The stellar flux in these windows was weighted by the inverse variance (as output from the reduction pipeline) and collapsed along the wavelength direction to obtain a stellar profile fitted with a Gaussian. The width and peak were used to estimate the S/N and FWHM for the blue

and red components of each alignment star. The average FWHM across a mask and the average star-by-star ratio of S/N values provide the seeing FWHM and *relative* S/N for that observation set. The typical spread in FWHM among stars on a given mask is 0.″03. The weight of each observation set was then given by $w = s/f^2$, where s is S/N and f is the FWHM, and these were normalized by the weights of all the coadded masks.

All emission line cutouts were inspected by eye and occasionally rejected if the region extended beyond the detector area or if there was an artifact in the data that could interfere with the line of interest. To perform the coaddition, each 2D cutout was first rectified to a regular grid in wavelength and spatial position using the 2D wavelength solution output by the spec2d pipeline. We located the peak of the continuum along the spatial axis by collapsing the 2D cutout in the wavelength direction, initially masking out the emission feature. The collapsed profile was fit by a Gaussian with the resulting peak taken as the galaxy center. In rare cases, the continuum was so weak that a position could not be determined without including flux from the emission line itself. The final centering of each cutout was verified by eye, and the cutouts were coadded with appropriate weighting after alignment in both wavelength and central continuum position.

The seeing varied from 0.″6 to 1.″2 over the various observing runs, so whenever seeing measurements are needed in the dynamical analysis (Section 3), we adopt the average value measured from the alignment stars in the final coadded observations. This measurement is preferred to that based on a photometric image, since it not only refers to data integrated over the entire exposure time of the spectra, but also accounts for systematics in the observing and coaddition process (which use different weights for different exposures).

2.3. Photometric Data and Bulge–Disk Decomposition

By selecting our sample within the GOODS North and South fields, we ensure excellent quality multi-color data for all our galaxies from *HST*/ACS (Giavalisco et al. 2004). This provides valuable structural information that can be used for translating the observed rotation curves into physically based properties. To the imaging in four bands from *HST* (B_{435}, V_{606}, i_{775}, and z_{850} -bands), we add ground-based K-band data in order to secure stellar mass estimates based on SED fitting (see Section 2.4).

A key requirement for our analysis is the inclination, P.A. and effective radius of each galaxy. We also need to separate, where possible, the disk light from bulge contamination. We derive these quantities from the *HST* imaging using the GALFIT3 (Peng 2010) least-squares elliptical-fitting method. For each galaxy we extracted a 9.″03 × 9.″03 (301 × 301 pixels) postage stamp centered on the object. Neighbors were individually masked out to eliminate confusion. We first fit an exponential disk component plus a de Vaucouleurs' bulge profile to every galaxy. Those galaxies which yielded unphysical solutions were refit with a single Sérsic profile component, where the Sérsic index (n) was allowed to vary. Such cases generally represent disk galaxies which are bulgeless and/or more clumpy and irregular than regular well-formed spirals. Approximately 60% of our galaxies were fit using a one-component n-varying Sérsic profile fit, and ∼40% were adequately fit with a two-component bulge and disk solution. This mixture gives some indication of the morphological distribution of our sample indicating that less than half are well-formed spirals (Section 2.1). Disk sizes, inclinations, and P.A.s were taken from best-fit disk components if more than one component can be fit. To track possible biases in the disk–bulge decomposition we will later flag those galaxies for which significant bulge components were measured.

We ran GALFIT using *HST* data in all four bands (B_{F435W}, V_{F606W}, i_{F775W}, and z_{F850LP}). The disk scale radii are consistent among the bands indicating no significant redshift-dependent bias (or *morphological k-correction*) within the sample. In order to maximize the S/N, hereafter we used the GALFIT results from the z_{F850LP} band. To achieve convergence on the GALFIT parameters and to assess any systematic uncertainty in the fitting technique, we ran a Monte Carlo analysis ($N = 1000$) where we varied the initial guess of each parameter (magnitude, effective radius, b/a for inclination, position angle, and sky) from one adopted by the GOODS SExtractor results (Giavalisco et al. 2004). We found that the parameter output distributions were much narrower than the input distributions, thereby demonstrating convergence. Final parameter uncertainties from the Monte Carlo distributions are better than 5% on average, and we add these uncertainties in quadrature to the observational error.

2.4. Stellar Masses

Reliable stellar masses are an essential component of constructing a baryonic TF relation. We take our stellar mass estimates from work initially presented in Bundy et al. (2005), followed by the analysis presented in Bundy et al. (2009). Further details can be found in those papers.

Briefly, stellar masses are derived using a matched catalog of multi-band ACS and ground-based K_S photometry. The essential near-infrared data was taken with the MOIRCS imager on the Subaru telescope for GOODS-N (Bundy et al. 2009) and the ISAAC instrument on the ESO Very Large Telescope (VLT) for GOODS-S (Retzlaff et al. 2010). The final matched catalog is substantially complete to a limiting magnitude of $K_{\rm AB} = 23.8$, deeper than our spectroscopic limit.

A Bayesian code fits the SED derived from 2″ diameter ACS and K_s photometry adopting the best spectroscopic redshift and this SED is compared to a grid of Bruzual & Charlot (2003) models that span a range of metallicities, star formation histories, ages and dust content. The stellar mass is estimated by multiplying the derived K-band mass/light ratio by the observed K-band luminosity derived from the `MAG_AUTO` total Kron magnitude determined by SExtractor. We assume a Chabrier (2003) IMF. The probability for each fit is marginalized over the grid of models giving a stellar mass posterior distribution function, the median of which is the catalogued value. At the magnitudes probed in this survey, the uncertainties inferred from the width of these posterior functions is less than 0.1 dex. Including systematic errors (see Bundy et al. 2005 for a full discussion), we determine that the stellar masses are reliable to better than 0.2 dex, modulo uncertainties arising from the IMF normalization.

In order to construct a self-consistent TF relation, we apply an aperture correction to the total stellar mass estimates (i.e., for a given fiducial radius, an aperture stellar mass at that radius compared to the velocity measured at that fiducial radius). We extract equivalent Kron radius aperture fluxes on the z_{F850LP} band data to get the flux equivalent to that used in the total stellar mass estimates. We then take a scaled-down aperture flux within the given fiducial radius, and compare this to the Kron radii flux, thus deriving a total-to-enclosed flux ratio. Assuming that the z_{F850LP}-band and K-band are roughly equivalent stellar tracers, we can use this ratio to estimate the enclosed stellar mass. This approach maximizes the utility of the *HST* z_{F850LP} images, which have much better resolution than our ground-based

K-band data, thereby giving us the resolved mass distribution throughout the disk to match the detail seen in our rotation curves.

3. DYNAMICAL ANALYSIS

We now turn to the questions of how to extract reliable rotation curves from our 2D spectroscopic data and how to interpret those curves in terms of a fiducial velocity measurement that can be used in the various TF relations we will example. To fully exploit our extended integrations, we reexamine the rotation curve model and consider carefully how to define a self-consistent fiducial velocity that can be robustly measured within our data. We quantify improvements in our data by comparing our velocities (extracted from 6–8 hr of integrated exposure time) with those deduced from ∼1 hr subsets, equivalent to exposures made in previous studies (Vogt et al. 1997; Conselice et al. 2005; Weiner et al. 2006b; Kassin et al. 2007). We also examine the remaining uncertainties given what has been learned from the first studies with IFU spectrographs. In what follows, our analysis is based on the 129 galaxies for which extended emission is observed (Section 2.2).

3.1. Rotation Curve Model

Optimally fitting rotation curves presents a variety of challenges that become more difficult as redshift increases. Foremost, we seek a functional form which represents the bulk of the observed emission line shapes and has some physical basis. Second, we must aim to characterize this functional form with a fiducial velocity that is reliably detected across the sample, preferably without extrapolation to radii where there is no data. Given our extended integrations, we have considered carefully the optimum selection of this characteristic velocity. The challenges can be appreciated by considering Figure 2 where we show various characteristic velocities in the context of the frequently used arctan model of a rotation curve (Courteau 1997) as well as the extent to which we can trace emission lines for our sample.

Several functional forms have been discussed in the literature, such as the "multi-parameter function" in Courteau (1997) and the "universal rotation curve" of Persic et al. (1996). The simplest model flexible enough to fit most rotation curves is the empirically motivated arctan function (see Figure 2), which we adopt here, viz:

$$V = V_0 + \frac{2}{\pi} V_a \arctan\left(\frac{r - r_0}{r_t}\right), \quad (1)$$

where V_0 is the central or systematic velocity, r_0 is the dynamic center, V_a is the asymptotic velocity, and r_t is the turnover radius, which is a transitional point between the rising and flattening part of the rotation curve (Courteau 1997; Willick 1999). The arctan model does not account for a sharp peak that is found in some local, bulge-dominated rotation curves around the turnover radius, but we typically do not observe this feature in our sample.

Past studies employed as TF velocities the maximum measured velocity along the disk, $V_{\rm max}$, or the asymptotic velocity from Equation (1), V_a (Vogt et al. 1996, 1997; Weiner et al. 2006b; Kassin et al. 2007). The disadvantage with $V_{\rm max}$ is that it is not measured at a consistent location in the variety of disks observed. In terms of the disk scale radius, we can see a range of a factor ≃5 or so in the associated radius.

Some studies (i.e., Flores et al. 2006; Weiner et al. 2006a) advocate the use of $V_{\rm circ}$, the circular radial velocity, driven by either the disk or the halo, but in nearly all cases this is assumed to be the V_a of the widely adopted arctan model. While the arctan function closely matches the observed extent of rotation curves, the mathematically extrapolated asymptote is unwarranted as it is not observed in typical data sets, even for our extended integrations. Small offsets in the extrapolated velocity curve will lead to large changes toward the asymptotic limit, especially when emission is not detected past the flattened part of the rotation curve, and emission line dispersion and seeing distort the terminal emission. Under these circumstances, the majority of the "$V_{\rm circ}$" velocities remain as extrapolations.

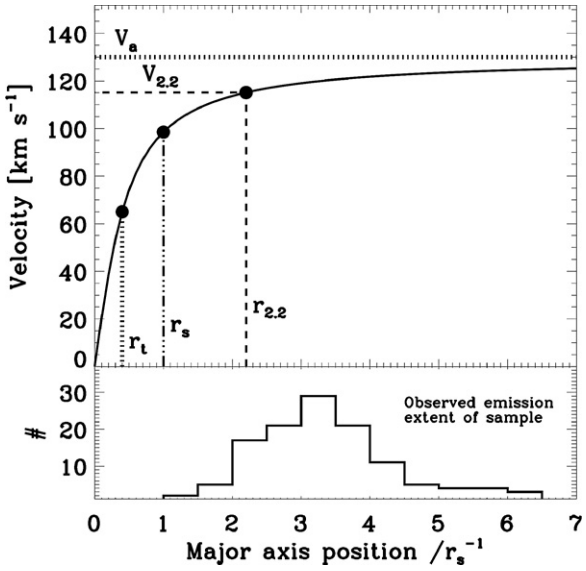

Figure 2. Functional arctan rotation curve with various characteristic radii (discussed in the text) shown as dimensionless factors of the disk scale length (r_s^{-1}). The example shown has a turnover radius, $r_t \sim 0.4\,r_s$, and an asymptotic velocity, $V_a \sim 130$ km s^{-1}, typical of many galaxies in our sample. The region where the rotation curve turns over is extensive and the so-called turnover radius, r_t, does not necessarily indicate the most appropriate center of this region for the arctan function. The histogram below shows the extent to which we can reliably trace emission lines in the spectra of our sample. The frequently used $V_{\rm max}$ (maximum measured velocity) is not equivalent to the asymptotic value, V_a, a mathematical extrapolation and typically not reached in the observed rotation curve. Estimates of V_a can depend critically on how well the central region and turn over of the rotation curve are constrained. As ∼90% of our galaxies are traced to $2.2r_s$ (and all to at least $1.0r_s$), in our TF relations we opt to use $V_{2.2}$, the velocity at $r_{2.2}$, which minimizes uncertainties arising from extrapolation (see Section 3.1).

We thus seek a physically motivated fiducial radius to which emission can be detected across the variety of disks seen over our wide redshift range. We have adopted the modeled velocity at 2.2 times the exponential disk scale length, $r_{2.2}$, which we will call $V_{2.2}$. This has a good physical basis as it corresponds to the location of peak rotational amplitude for a pure exponential disk (Freeman 1970; Binney & Tremaine 1987; Courteau & Rix 1997). Although few disks are likely to be perfectly exponential, the $r_{2.2}$ approximation as the point at which rotation curves flatten is visually confirmed in most of our galaxies. TF velocities based upon $V_{2.2}$ result in the smallest internal scatter and provide the best match to radio (21 cm) line widths for local galaxies (Courteau 1997). This fiducial velocity has been adopted by Dutton et al. (2010) in determining the kinematic connection between late-type galaxies and dark matter halos. As shown in Figure 2 we trace the velocity field with at least one optical emission line to $r_{2.2}$ for ∼90% of our sample (Figure 2).

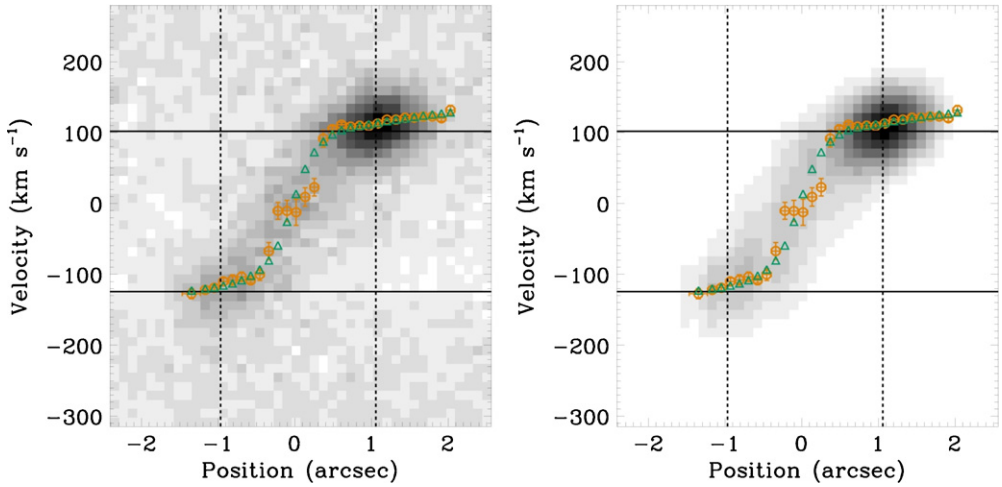

Figure 3. Example of our fitting procedure for a galaxy with asymmetric emission. The left panel shows the observed 2D spectral data in the region of $H\alpha$, and the right panel is the equivalent section of the constructed model spectrum. Both show a gray scale representing flux as a function of velocity with respect to position. Orange circles show the trace centroids of the emission line (bars along the positional dimension indicate bin size, not error), and the green triangles show the equivalent centroids for the constructed model. The $r_{2.2}$ radius is marked by vertical dotted lines and the extracted $V_{2.2}$ velocity is marked by horizontal solid lines. These lines of fiducial measurements do not cross directly through the trace because they are extracted from the best-fit model's intrinsic arctan function, prior to distortion by seeing and dispersion. See Section 3.2 for more details.

3.2. Rotation Curve Fitting Procedure

We now discuss how we fit the emission line data to obtain an accurate velocity measurement at $r_{2.2}$ for each galaxy disk using the arctan model. In the next section we discuss various inclination corrections that must be made following the fitting procedure. A simple outline of our fitting code is as follows.

1. Trace the observed 2D emission line in wavelength as a function of spatial position,
2. Construct a model 2D spectrum with an arctan-shaped emission line profile, implementing features measured from step 1 (e.g., position-dependent emission brightness profile, dispersion, and seeing),
3. Trace the model spectrum, varying the arctan model parameters V_a and r_t (as well as the dynamical center and a seeing-dispersion beam correction factor) until the model trace optimally fits that of the data,
4. Compute $V_{2.2}$ at $r_{2.2}$ from the best-fit arctan models.

In detail, our procedure is as follows.

Step 1. We begin by subtracting the galaxy continuum on the rectified 2D spectral frame, leaving only the emission-line profile. This is performed by linearly interpolating in wavelength across the emission line region, treating each spatial row independently.

Step 2. We next trace each emission line as a function of spatial position. This procedure returns the central wavelength, line width, and peak flux in each spatial bin. We fit two half-Gaussians to the line profile in the wavelength direction, and use an adaptive binning procedure in the spatial direction to ensure a consistent S/N. The blurring effect of seeing in the spatial direction, and of dispersion in the wavelength direction, can affect the emission line in a particular spatial bin by mixing flux from neighboring bins. We use two half-Gaussians with differing sigmas joined at the same peak to account for these effects, ensuring that the position of the peak flux is always traced.

The trace terminates when the emission is no longer detected above the local noise level. All traces are visually inspected to ensure that spurious reduction artifacts do not interfere with the fit. The procedure produces an array of wavelength values as a function of spatial position (see Figure 3), as well as the emission peak flux.

We also experimented with different forms for the emission line brightness profile along the slit, for example the collapsed light through a synthetic slit estimated from the *HST* image, or an exponential profile. However, traces using these profiles resulted in larger residuals.

Step 3. We next construct a model 2D spectrum from the rotation curve of Equation (1), which requires V_a and r_t parameters for the arctan functional form. We guess initial values to approximately match the flat portion of the outer trace of the observed data. We lay this model rotation curve on a 2D grid, adjusting the normalization (brightness) and line width in each spatial bin to match that of the data (i.e., using the parameters from the two half-Gaussians in each bin). We finally convolve the resulting rotation curve with the local seeing (see Section 2.2 for details), and the resulting peak model brightness is re-normalized, bin by bin, to that observed. Ideally we would start with the unblurred emission-brightness spatial profile, but there is a degeneracy in blurring by seeing and dispersion, which is particularly troublesome for galaxies with irregular emission line brightness profiles.

Because we have measured the position-dependent dispersion from the trace (which implicitly contains the effect of the seeing), as well as a separate measurement of the seeing from the alignment stars, we can attempt to break this degeneracy by fitting for a multiplicative factor. This correction factor is used to multiply the dispersion implemented in the model, and it is always less than or equal to 1. This allows us to approach the intrinsic, deconvolved rotation curve. This method is more successful than alternative approaches we attempted using both synthetic and observed data, for example adopting the collapsed light profile from the most appropriate broadband *HST* image as observed through the slit, or simple functional forms of emission brightness profiles (constant, linear, exponential). Indeed, we find many emission lines that are brighter at the disk edge than toward the center, as well as asymmetric emission distributions which do not match the broadband flux distributions that enter the slit.

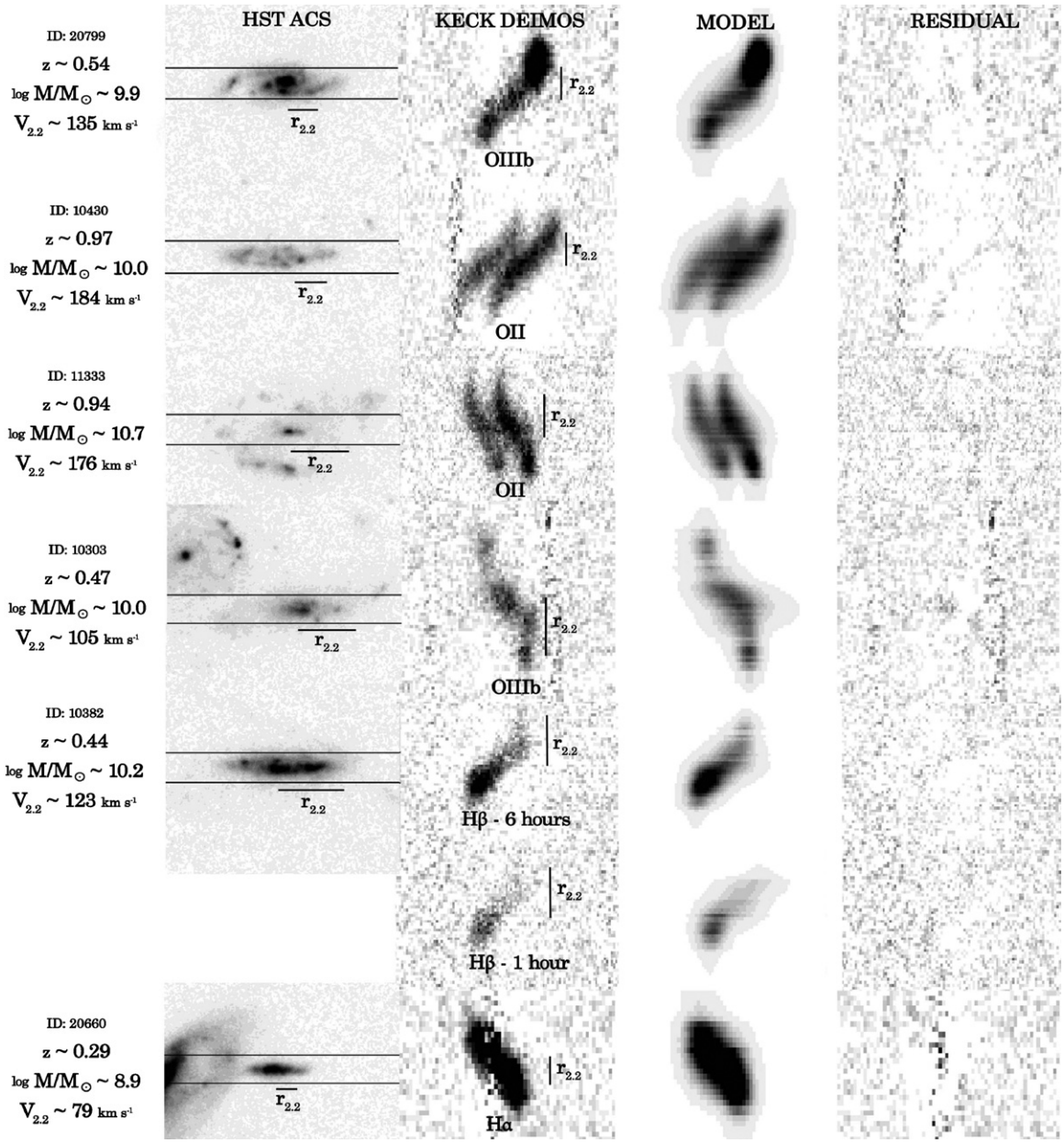

Figure 4. Examples of data from the survey. For each source we show an *HST*/ACS composite (B, V, i, z) photometry postage stamp rotated for convenience so the overlaid 1″ slit level is horizontal, the Keck DEIMOS 2D emission line cutout, the corresponding best model and residual of model minus data. The extent of $r_2.2$, where $V_{2.2}$ is measured is also overlaid. The triptych second to the bottom shows the same emission line as the one above but with only 1 hr spectroscopic integration.

Step 4. To select the best model, we use a robust nonlinear least-squares fitting algorithm based on MPFIT (Markwardt 2009). The arctan input parameters, V_a and r_t are varied as well as the position of the dynamical center and the seeing-dispersion beam correction factor. Chi-squares are calculated between the model trace and the data trace, rather than on the entire 2D frame. Not only is this method much faster, but we find it results in smaller residuals, simply because we are focusing the fit on the information that is most important to the shape of the rotation curve. We propagate the error from the measured input parameters (emission profile, seeing, and dispersion) by using a Monte Carlo approach, simultaneously altering input parameters from random Gaussian distributions with widths matching the error in the observed parameters for each galaxy. After 100 iterations, we add the uncertainty from the resulting distribution of output velocities to the formal fitting errors.

The velocity at $r_{2.2}$ can then be calculated using the best-fit arctan model and the radius measured from the z_{F850LP} band *HST* data (see Section 2.3). All the observed emission lines in a given spectrum are treated independently in the above steps. These independent measurements of $V_{2.2}$ are found to be consistent in >90% of our galaxies. We combine the emission line fits for the same galaxy into a final weighted average of $V_{2.2}$ and include the error in $r_{2.2}$ in the final uncertainty.

Examples of our spectral data and respective best-fit model rotation curves can be found in Figures 4 and 5. Note that these models represent the minimum χ^2 best-fit on the 1D trace of the 2D models as described above, not a direct 2D χ^2 best-fit. Figure 4 shows six examples of disks which appear mostly morphologically regular in their *HST* multi-filter photometry, whereas Figure 5 displays six galaxies which are likely more disturbed or irregular based on their *HST* images. In both

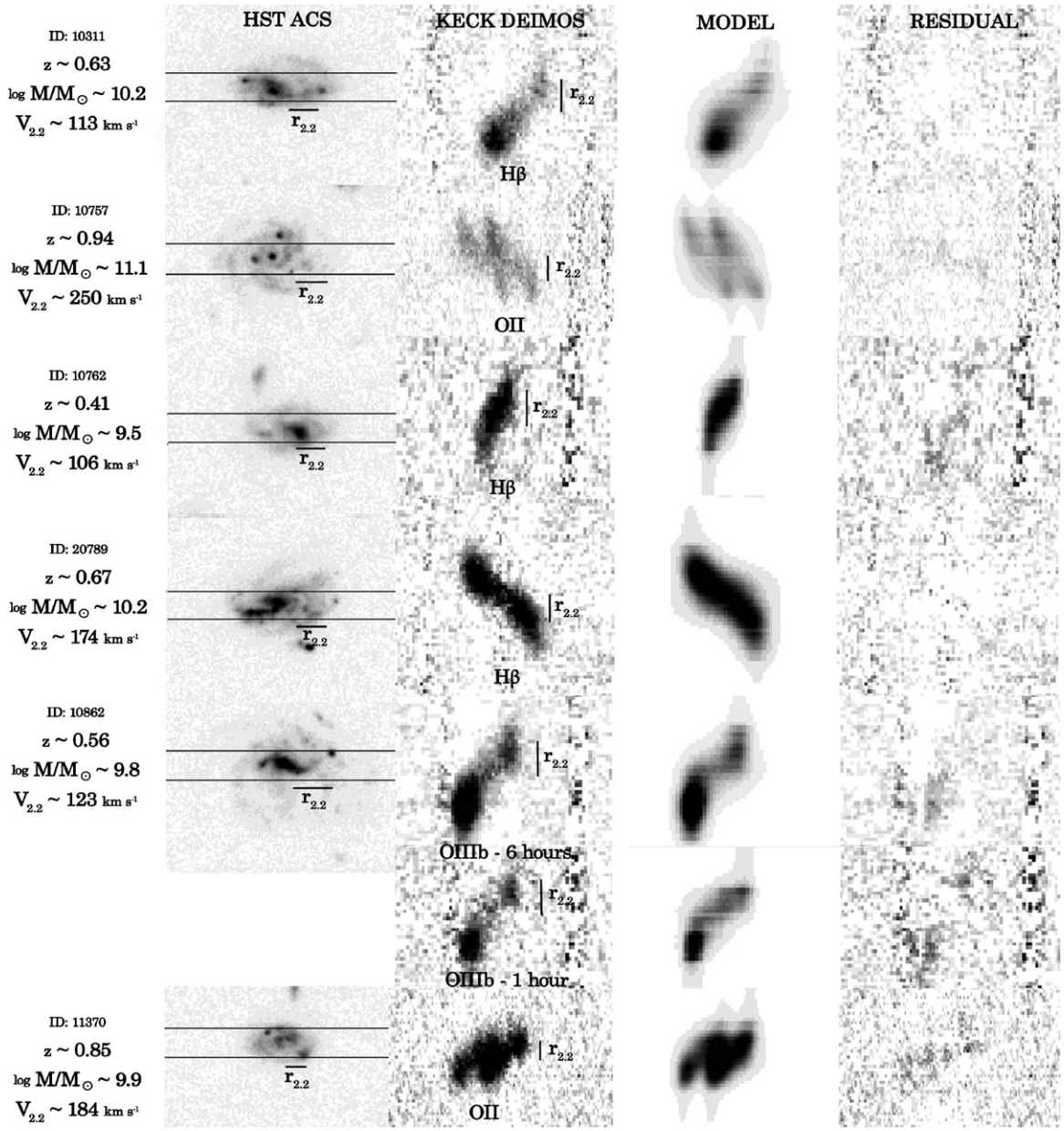

Figure 5. As Figure 4 but for more disturbed, visually asymmetric disks, some of which appear to be undergoing minor mergers. Although the morphologies are more irregular, we usually succeed in fitting an appropriate arctan-based model.

figure sets, we observe fairly regular arctan-shaped kinematics, although places of high dispersion and brightness in the emission line tend to coincide with regions of the galaxy in the *HST* image that appear to be internally or externally disturbed. For the fifth galaxy in both figures, we show the best-fit model rotation curve after only 1 hr of integration time for a comparison to the full 6–8 hr of integration shown in the panel just above.

3.3. Inclination and P.A. Offset Corrections

We now correct our $V_{2.2}$ measurements for the effects of disk inclination and any misalignment between the P.A. of the DEIMOS slit and the major axis of the galaxy as determined from GALFIT.

Adopting the convention $i = 0°$ for face-on and $i = 90°$ for edge-on disks, the inclination correction is

$$V_{\rm corr} = \frac{V_{\rm obs}}{(\sin i)}, \tag{2}$$

$$i = \cos^{-1}\sqrt{\frac{(b/a)^2 - q_0^2}{1 - q_0^2}}, \tag{3}$$

where $q_0 \simeq 0.1$–0.2 represents the intrinsic flattening ratio of an edge-on galaxy (Haynes & Giovanelli 1984; Courteau 1996; Tully et al. 1998). Although the precise value depends on morphology, the uncertainty leads to changes in the final velocity measurement on the order of 1 km s^{-1} (Pizagno et al. 2005; Haynes & Giovanelli 1984). We assumed $q_0 = 0.19$ for all systems, similar to Pizagno et al. (2005).

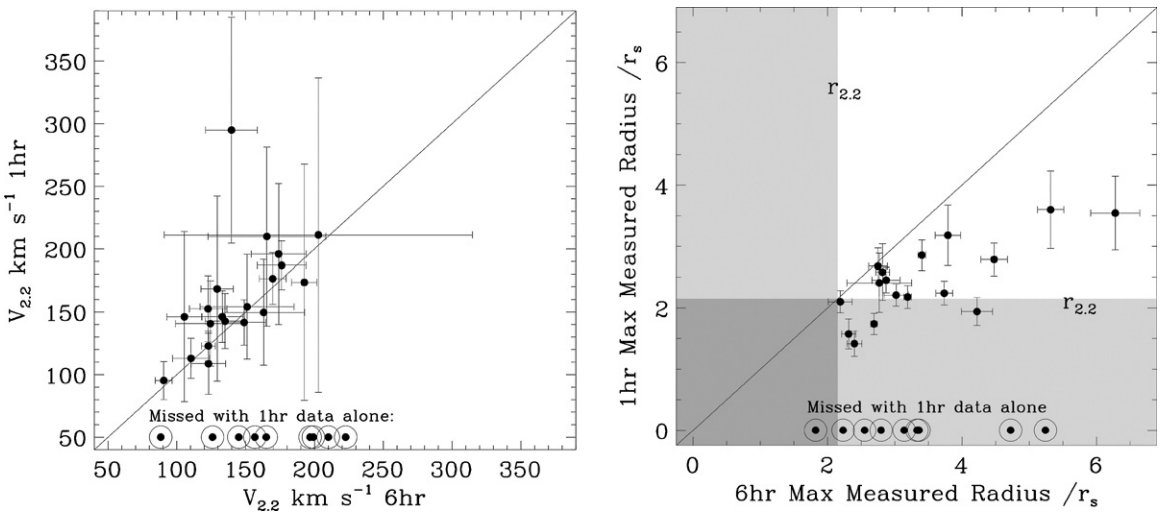

Figure 6. Comparison of the modeled $V_{2.2}$ values and maximum measured emission line extent as derived from our total exposure time (6 hr in these examples) to those derived from a 1 hr exposure extracted as a subset of our data. Left: the agreement between $V_{2.2}$ values is reasonable given the errors; however, there is a systematic offset and the errors are significantly larger for the 1 hr subset. Right: almost every galaxy reveals significantly more extended emission in the 6 hr data. The shading marks the $r < r_{2.2}$ region; if the emission does not extend beyond this region, $V_{2.2}$ must be extrapolated, as is the case for several 1 hr galaxies. Note also that a third of the rotation curves cannot be adequately traced with only 1 hr of integration (circled points).

For the P.A. offset, we determine a correction

$$V_{\rm corr} = \frac{V_{\rm obs}}{\cos(\Delta {\rm P.A.})} \quad (4)$$

from simple trigonometry accounting only for the misaligned slit component of the true major axis. Only 10 galaxies in our final sample have velocity corrections arising from a P.A. offset greater than 10%, and no P.A. offset exceeds 45°.

We apply these two corrections to produce a catalog of corrected $V_{2.2}$ measurements, where the effects of seeing, velocity dispersion and the emission line brightness profile are accounted for in the model (see Table 2). As explained in Section 2.4, to compare like with like in our TF relations, we match $V_{2.2}$ to an estimate of the stellar mass within $r_{2.2}$. In order to compare this *enclosed* relation to a more familiar construction of the TF relation used in previous studies, we also consider a *total* relation, which compares the stellar mass estimated from the Kron radius with the velocity associated with the optical radius r_D, defined for an exponential profile as one enclosing ∼83% of the light, or $3.2r_s$. This measurement of $V_{3.2}$ or V_D we find to be comparable to the $V_{\rm circ}$ or $V_{\rm max}$ of previous intermediate-redshift studies; however, our choice of r_D is more consistent between disks than the $r_{\rm max}$ used in those studies.

3.4. Demonstrating the Advantages of Extended Integrations

A major advance in our survey is the use of extended integration times (typically 6–8 hr) on sources with apparent magnitudes ($z_{F850LP} < 22.5$) that have typically been observed for ∼1 hr of exposure time (Vogt et al. 1997; Conselice et al. 2005; Weiner et al. 2006b; Kassin et al. 2007). In addition to ensuring our emission lines are traced to $r_{2.2}$ (Figure 2), this leads to improved S/N at all radii. We can demonstrate the effect this has on our derived velocities by using our model fitting code on a subset of our data taken with a 1 hr integration time. Comparing the results with the 6 hr integrations in Figure 6, we can draw two important conclusions.

First, while most $V_{2.2}$ measurements are consistent given the error bars, the 1 hr data has significantly larger error bars and there is a systematic offset whereby the 1 hr analysis produces on average a 13% higher measurement of $V_{2.2}$ than the 6 hr data. This suggests that if errors are not properly accounted for, studies using a similar modeling procedure but with less integration time may falsely detect evolutionary signals as a result of overestimated velocities due to the decline in S/N.

Second, as expected, the 6 hr data enables us to probe largely beyond $r_{2.2}$, whereas this is not the case for the 1 hr subset. The right-hand panel in Figure 6 shows the gains made in detected emission extent in factors of scale radius. We trace, on average, 30% further along the disk with the 6 hr data than the 1 hr data. In fact, modeling an arctan function fails for one-third of the 1 hr sample due to the low S/N, and missing segments of the emission create a false deviation from the arctan shape. We are confident that we have successfully converged on necessary integration time in our 6 hr data because emission is traced beyond $r_{2.2}$ in ∼90% of our disks, ensuring we can accurately measure $V_{2.2}$.

3.5. Comparison to Previous Work

Our rotation curve fitting method was constructed to work on data with extended exposure times, so it is interesting to compare it to velocities for the same galaxies derived using alternative techniques. The greatest overlap can be found using the TKRS/GOODS sample (Wirth et al. 2004; Giavalisco et al. 2004). Figure 7 shows 35 of our galaxies in common with the TKRS/GOODS sample for which there are 2D spectral fits for $V_{\rm rot}$ (equivalent to V_a and does not include a correction for inclination), and all of our sample overlaps with their 1D line-width measurements (Weiner et al. 2006a, 2006b). We compare the velocities we measure for these galaxies without the inclination correction applied for a most direct comparison.

On average, the mean $V_{\rm rot}$ for the TKRS 2D data is 68% of the mean $V_{2.2}$ for our study. For the 1d line-width data, the TKRS measurements have a mean that is 75% of the $V_{2.2}$ mean in our study. Our current data have significantly smaller error bars as would be expected given the longer integration times: the median fractional error bar is 8.6% for this study, and 59.1% for TKRS.

Table 2
Table of Measurements

R.A.	Decl.	z	m_z	P.A.$_{\rm slit}$[a]	P.A.$_{\rm off}$[b]	$\sin(i)$[c]	$r_{2.2}$[d]	$M_*(r_{2.2})$[e]	M_B[f]	M_{K_s}[g]	$V_{2.2}$[h]	$V_{\rm slit}$[i]	Lower $M_{\rm dyn}$[j]	Upper $M_{\rm dyn}$[k]
189.28400	62.204340	0.59	22.22	36.10	0.00	0.97	2.87 ± 0.21	9.44 ± 0.17	19.83 ± 0.56	22.76 ± 0.64	67.55 ± 10.02	29.92	9.36 ± 0.11	9.80 ± 0.11
189.34309	62.196030	0.53	21.97	81.30	0.73	0.96	5.26 ± 0.19	9.11 ± 0.14	19.76 ± 0.48	22.41 ± 0.54	66.07 ± 6.31	16.26	9.60 ± 0.07	9.92 ± 0.07
189.32520	62.213470	0.91	22.17	36.70	0.02	0.96	10.73 ± 0.54	10.77 ± 0.03	20.82 ± 0.10	24.97 ± 0.10	227.47 ± 39.66	10.26	10.99 ± 0.13	11.15 ± 0.13
189.38380	62.212980	1.02	21.22	76.40	0.02	0.79	13.84 ± 0.24	11.40 ± 0.12	22.17 ± 0.36	26.23 ± 0.43	260.36 ± 51.88	12.74	11.21 ± 0.14	11.38 ± 0.14
189.33160	62.215710	0.91	22.47	54.30	0.00	0.86	3.64 ± 0.23	10.41 ± 0.04	20.66 ± 0.13	24.62 ± 0.13	129.87 ± 69.84	34.05	10.03 ± 0.63	10.36 ± 0.63
189.40388	62.242610	0.63	21.39	66.00	0.09	0.93	8.31 ± 0.21	9.95 ± 0.18	20.64 ± 0.57	23.49 ± 0.65	99.18 ± 6.13	13.82	10.15 ± 0.04	10.39 ± 0.04
189.44249	62.244660	0.64	21.49	72.30	0.04	0.84	3.33 ± 0.21	10.31 ± 0.06	20.55 ± 0.12	24.38 ± 0.15	175.47 ± 14.38	33.86	10.25 ± 0.06	10.53 ± 0.06
189.30710	62.253220	0.52	21.03	43.80	0.00	0.88	4.24 ± 0.19	10.29 ± 0.06	20.29 ± 0.18	24.13 ± 0.21	181.54 ± 29.76	28.62	10.39 ± 0.12	10.64 ± 0.12
189.33580	62.274980	0.84	21.59	72.20	0.03	0.88	8.22 ± 0.23	10.05 ± 0.18	21.28 ± 0.58	24.09 ± 0.65	168.61 ± 4.61	18.26	10.61 ± 0.02	10.82 ± 0.02
189.21300	62.175340	0.41	19.94	36.10	0.18	0.56	4.04 ± 0.16	10.59 ± 0.06	20.46 ± 0.18	24.70 ± 0.22	170.26 ± 10.68	27.67	10.31 ± 0.04	10.57 ± 0.04
189.17271	62.181010	0.94	22.47	73.50	0.12	0.96	5.48 ± 0.24	10.34 ± 0.06	20.65 ± 0.19	23.74 ± 0.20	171.56 ± 43.62	20.06	10.45 ± 0.20	10.67 ± 0.20
189.22171	62.188090	0.94	21.27	73.40	0.22	0.64	7.96 ± 0.24	10.86 ± 0.05	21.72 ± 0.16	25.64 ± 0.19	228.84 ± 34.51	21.64	10.86 ± 0.11	11.07 ± 0.11
189.29829	62.190790	0.41	21.81	26.20	0.06	0.84	5.63 ± 0.37	9.30 ± 0.10	19.01 ± 0.33	21.57 ± 0.37	86.23 ± 4.70	20.20	9.86 ± 0.05	10.17 ± 0.05
189.27409	62.257080	0.50	21.86	58.90	0.04	0.76	5.83 ± 0.18	9.59 ± 0.09	19.51 ± 0.28	22.40 ± 0.32	116.64 ± 17.25	23.41	10.14 ± 0.10	10.42 ± 0.10
189.06029	62.121890	0.97	21.25	79.70	0.15	0.50	10.87 ± 0.24	11.05 ± 0.03	22.24 ± 0.11	25.20 ± 0.12	236.10 ± 9.21	14.03	11.02 ± 0.03	11.20 ± 0.03
189.15370	62.126510	1.00	22.10	79.00	0.00	0.61	6.60 ± 0.24	10.20 ± 0.19	21.90 ± 0.64	24.80 ± 0.73	169.74 ± 65.96	26.13	10.52 ± 0.35	10.77 ± 0.35
189.05609	62.153080	0.41	20.59	64.90	0.02	0.80	5.99 ± 0.20	10.01 ± 0.06	20.21 ± 0.20	23.20 ± 0.23	120.14 ± 8.35	19.79	10.18 ± 0.05	10.44 ± 0.05
189.02771	62.164350	1.20	21.07	45.20	0.02	0.99	24.31 ± 0.25	11.06 ± 0.03	20.66 ± 0.11	25.25 ± 0.11	219.27 ± 39.61	1.78	11.31 ± 0.13	11.44 ± 0.13
189.11980	62.173260	0.94	21.88	37.70	0.38	0.82	17.76 ± 0.73	10.66 ± 0.05	21.27 ± 0.17	24.44 ± 0.20	167.54 ± 8.68	9.51	10.94 ± 0.04	11.11 ± 0.04
189.15421	62.199970	0.78	21.38	79.50	0.06	0.65	9.16 ± 0.22	10.12 ± 0.17	21.24 ± 0.55	24.09 ± 0.62	141.64 ± 12.20	17.87	10.51 ± 0.06	10.73 ± 0.06

Notes.
[a] In degrees.
[b] In radians.
[c] sin of inclination.
[d] 2.2 × scale radius in kpc.
[e] Enclosed stellar mass in log $M_*/M_\odot$ dex.
[f] Total absolute B-magnitude in mags.
[g] Total absolute K-magnitude in mags.
[h] Best modeled velocity at $r_{2.2}$ in km s^{-1}.
[i] Estimate of upper limit of velocity broadening of slit, in km s^{-1}.
[j] Enclosed dynamical mass in log $M_*/M_\odot$ dex, lower limit (without slit effects correction, assuming an oblated potential where $q = 0.4$).
[k] Enclosed dynamical mass in log $M_*/M_\odot$ dex, upper limit (with slit effects correction, assuming a spherical potential).

(This table is available in its entirety in a machine-readable form in the online journal. A portion is shown here for guidance regarding its form and content.)

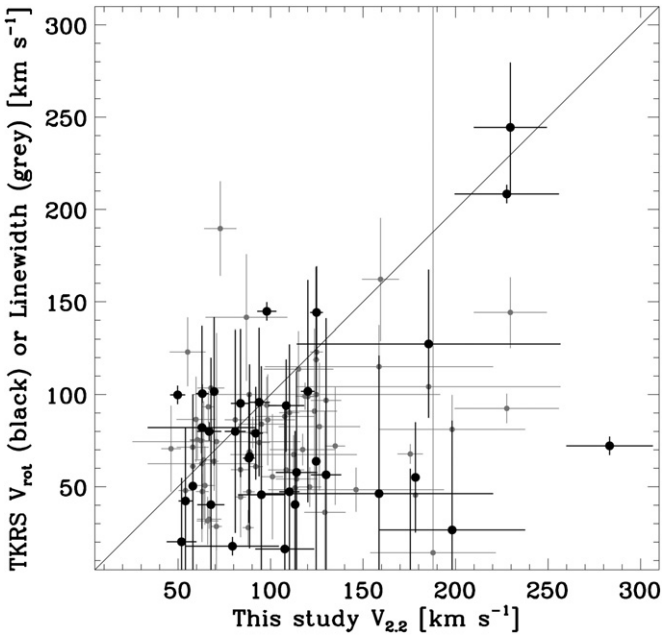

Figure 7. Comparison of the velocities for 35 galaxies that overlap between this study and the TKRS/GOODS study of Wirth et al. (2004) and Giavalisco et al. (2004). In black are shown the TKRS/GOODS 2D spectral fits for $V_{\rm rot}$ (equivalent to V_a), and in gray are the TKRS/GOODS 1D line-width measurements. Inclination corrections are not applied to any of the velocity measurements plotted here.

The three galaxies in common with the Flores et al. (2006) and Puech et al. (2008) studies have consistent velocity measurements within the error bars when comparing only the equivalent slit area from our study to their modeled IFU data. One galaxy has an inconsistent TF velocity measurement since a higher $V_{\rm max}$ is found on either side of the slit area on the full modeled IFU velocity field. Little can be concluded from a comparison of three objects; however, in terms of sample selection, it is encouraging that the three shared objects between our studies all belong to the sub-class of *Complex Kinematics* in the Flores et al. (2006) kinematical classification scheme, consisting of objects with the most irregular, peculiar observed kinematics.

4. RESULTS

We now reach the primary aim of our paper: to present the redshift-dependent M_*-TF relation over $0.2 < z < 1.3$. We will explore the quantitative improvement, which we have realized through our extended integrations and subsequent rotation curve modeling, with respect to earlier work in a number of ways. Foremost, the scatter around the redshift-dependent relations will provide a good indication of our progress. We will examine relations using masses derived within our chosen fiducial 2.2 scale radius, $r_{2.2}$, the so-called *enclosed* relations alongside those for the more traditional *total* relations (see Section 2.4 and the end of Section 3.1 for more details). It is also convenient to examine and discuss the B-band luminosity-based TF relation from our survey as the literature contains many estimates of this scaling relation and previous studies have claimed evolution, despite large scatter and possible incompleteness biases (Section 4.2).

4.1. The Redshift-dependent Stellar Mass TF Relation

We begin by considering the case for evolution in the M_*-TF relation. The results are illustrated in Figure 8 and listed in Table 3. Redshift bins were selected to ensure nearly uniform samples over our total redshift range. Shifting the boundaries of these bins by modest amounts does not change the overall conclusions we present below.

To fit a linear regression to our data we adopt a least-squares approach that incorporates a measurement of the intrinsic scatter $\sigma_{\rm int}$, which is added in quadrature to the velocity dimension. We fit a zero-pointed line:

$$\log(M_*) = [a + b\log(V_{2.2})] - \log(M_0), \quad (5)$$

where $M_0 = 10^{10} M_\odot$, and while we plot the relation in the familiar way with velocity on the x-axis and a y-intercept given in terms of stellar mass, we treat velocity as the dependent variable in the linear regression. Fitting linear regressions with stellar mass as the dependent variable leads to fits which suffer much more from the effects of incompleteness bias (Bamford et al. 2006; Weiner et al. 2006a; Kelly 2007).

To fit the data to Equation (5), we adapted a code which takes into account errors in both the ordinate and abscissa. We first fit an unrestricted slope to the entire, un-binned log V–M_* data set, and then fit the individual redshift-binned relations with a distribution of slopes drawn from a Monte Carlo ($N = 100$) Gaussian distribution of slopes centered on the slope found for the full sample. We undertake this exercise for both the *enclosed* mass (i.e., that associated with our fiducial radius, $r_{2.2}$), and the *total* mass. We also experiment with simpler approaches to linear regressions, which result in similar trends but naively smaller errors, so we present here our most robust results with the broadest consideration of the uncertainties.

For a local comparison, we consider the M_*-TF relation derived from K-band luminosities published by Bell & de Jong (2001) and the M_*-TF relation from Pizagno et al. (2005), the latter of which is based on velocities from $r_{2.2}$ as presented in the enclosed relation of this study.

Before discussing possible evolution, we consider the derived scatter around the relations since this is a valuable indication of our gains in precision. Satisfactorily, we find intrinsic scatters in the fits of 0.055, 0.067, 0.055 (dex of V km s^{-1}) at $\langle z \rangle = 0.37$, 0.62, 0.96, which are comparable to that seen in local TF relations (i.e., ∼0.049 in Pizagno et al. 2005). Our analysis therefore represents a significant improvement on the scatter seen in earlier intermediate-redshift studies, for example an improvement by a factor of two to three over the study of Conselice et al. (2005). We also achieve a scatter less than that found in the M_*–$S_{0.5}$ relation of Kassin et al. (2007; between 0.08 and 0.11 dex), despite the fact that they introduce an additional dispersion term, $S_{0.5}$, which significantly tightens the relation from the log V–M_* relation.

Table 3 shows little room for evolution in the relation. Fitting a straight line through the zero points between redshift bins, we detect a modest but statistically insignificant trend for a larger stellar mass at fixed velocity at lower redshift: $\Delta M_* \sim 0.037 \pm 0.065$ dex (1σ) from $\langle z \rangle \sim 1.0$ to 0.3. Fitting a straight line through zero points between redshift bins in the Conselice et al. (2005) study, we see a $\Delta M_* \sim 0.07 \pm 0.19$ dex (1σ) from $\langle z \rangle \sim 1.0$ to 0.3, consistent with our result, yet more uncertain. Interestingly, our 1σ limit for evolution is consistent with the modest $\Delta \log M_*/M_\odot$ predicted by Portinari & Sommer-Larsen (2007; $\Delta M_* \sim 0.1$), Somerville et al. (2008; 10% decrease in V at fixed M_* with time), and only consistent with Dutton et al. (2011a; $\Delta M_* \sim 0.2$) over a similar redshift range at the 2σ level. Importantly, this result is robust to the inclusion of the

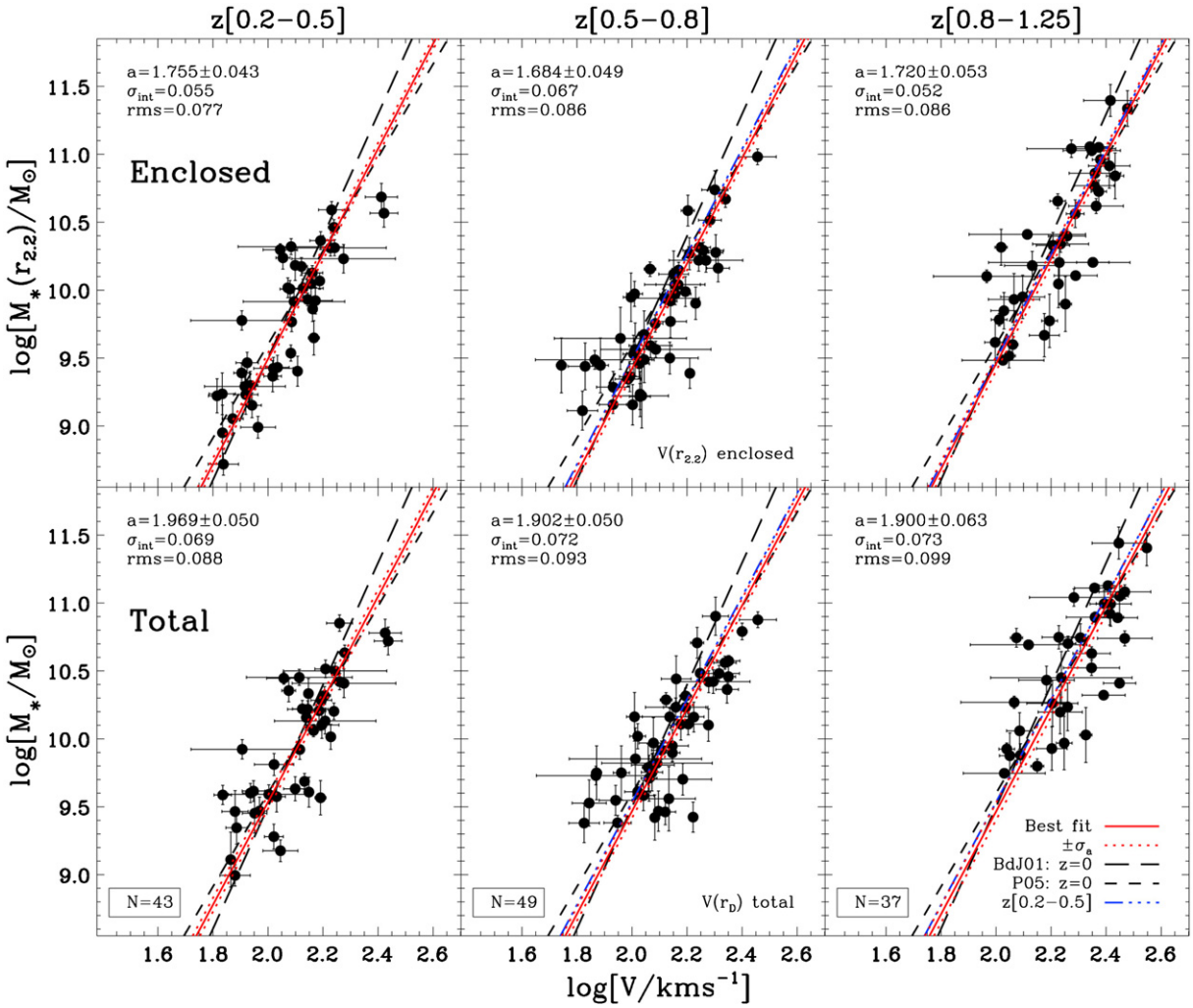

Figure 8. Redshift-dependent stellar mass Tully–Fisher (M_*-TF) relations using the enclosed (top panels) and total (bottom panels) mass estimates. Dashed lines refer to the local relations of Bell & de Jong (2001) and Pizagno et al. (2005). Dot-dashed lines refer to the fit to the lowest-redshift bin in the current data set. To fit fixed slopes between redshift bins, we fit relations using a Monte Carlo distribution of slopes from the best-fit free slope of the entire sample. The resulting mean slope is shown as a solid red line with red dotted lines showing the 1σ error in the zero point (in $M_*/M_\odot$ dex). Using the velocity and enclosed mass at the $r_{2.2}$ aperture reduces both the intrinsic scatter ($\sigma_{\rm int}$) and the rms of the relationship in each redshift bin.

Table 3
Stellar Mass Tully–Fisher Relations

z Range	$\langle z \rangle$	N	a[a]	b[b]	$\sigma_{{\rm int},V}$[c]	Median σ_V[d]	rms$_V$[e]	$\sigma_{{\rm int},M}$[f]	Median σ_M[g]	rms$_M$[h]
Enclosed: $M_*(r_{2.2})$ vs. $V(r_{2.2})$:										
$0.2 < z \leqslant 1.3$	**0.64**	**129**	**1.718**	**3.869**	**0.058**	**0.022**	**0.083**	**0.224**	**0.091**	**0.323**
$0.2 < z \leqslant 0.5$	0.37	43	1.755 ± 0.043	" fixed	0.055	0.035	0.077	0.211	0.081	0.297
$0.5 < z \leqslant 0.8$	0.62	49	1.684 ± 0.049	" fixed	0.067	0.045	0.086	0.257	0.118	0.334
$0.8 < z \leqslant 1.3$	0.96	37	1.720 ± 0.053	" fixed	0.052	0.062	0.086	0.202	0.098	0.331
Total: M_* vs. $V(r_D)$										
$0.2 < z \leqslant 1.3$	**0.64**	**129**	**1.926**	**3.783**	**0.070**	**0.023**	**0.093**	**0.266**	**0.087**	**0.353**
$0.2 < z \leqslant 0.5$	0.37	43	1.969 ± 0.050	" fixed	0.069	0.037	0.088	0.262	0.083	0.332
$0.5 < z \leqslant 0.8$	0.62	49	1.902 ± 0.050	" fixed	0.072	0.057	0.093	0.272	0.110	0.351
$0.8 < z \leqslant 1.3$	0.96	37	1.900 ± 0.063	" fixed	0.073	0.064	0.099	0.277	0.084	0.375

Notes.
[a] Best-fit y-intercept in $M_*/M_\odot$ dex assuming scatter in $V/{\rm km\,s^{-1}}$ dex.
[b] Slope assuming scatter in $V/{\rm km\,s^{-1}}$ dex.
[c] Internal scatter in $V/{\rm km\,s^{-1}}$ dex.
[d] Median velocity error in $V/{\rm km\,s^{-1}}$ dex.
[e] Total scatter in $V/{\rm km\,s^{-1}}$ dex.
[f] Internal scatter in $M_*/M_\odot$ dex.
[g] Median stellar mass error in $M_*/M_\odot$ dex.
[h] Total scatter in $M_*/M_\odot$ dex.

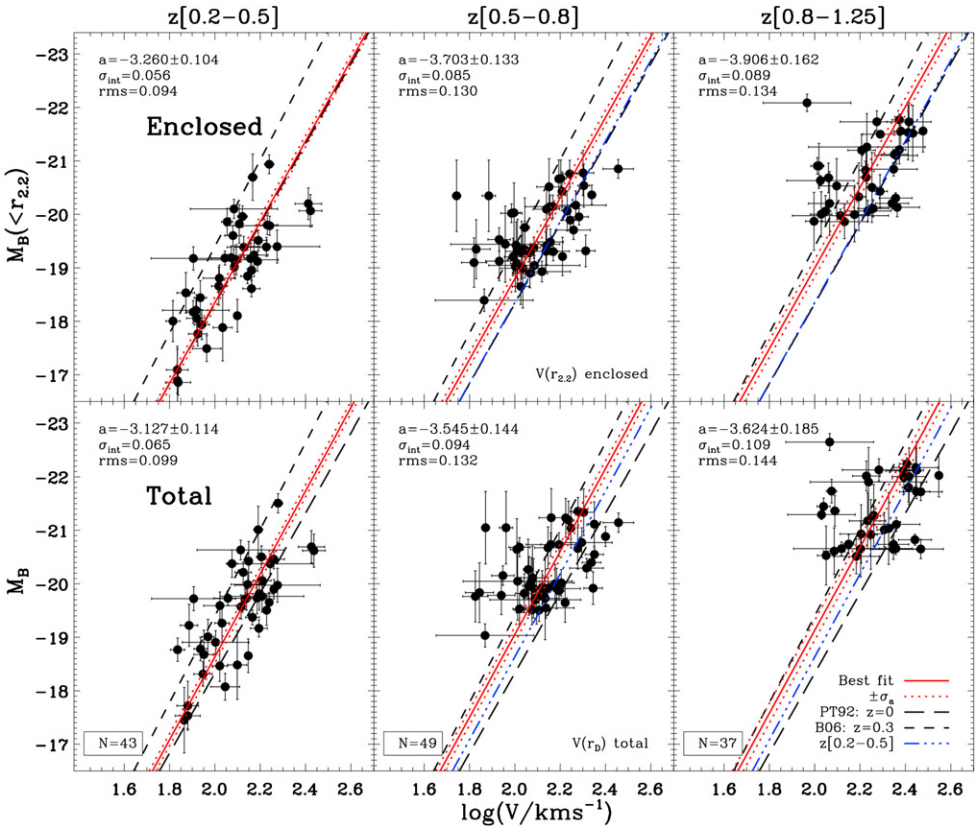

Figure 9. As Figure 8 but for the absolute B-band magnitude (M_B) Tully–Fisher relation. For comparison purposes, we show the local relation of Pierce & Tully (1992) and the $z \sim \langle 0.3 \rangle$ relation of Bamford et al. (2006) as dashed lines. Other lines are as in Figure 8.

local data in both the *enclosed* and *total* relations. We discuss the implications of this agreement further in Section 5.

We note that the scatter in the *total* M_*-TF relations is increased somewhat compared to that in our preferred *enclosed* relations, most likely due to the effect of extrapolated velocity measurements. We trace spectroscopic emission beyond r_D on ∼60% of our disks as opposed to ∼90% beyond $r_{2.2}$.

4.2. The B-band Magnitude TF Relation

We undertake a similar analysis to that described in Section 4.1 for the absolute B-magnitude TF (M_B-TF) relation, where M_B measurements come from the best-fit SEDs (described in Section 2.4), and are aperture corrected in the same way as the stellar mass estimates. The TF relations are shown in Figure 9 for both total and enclosed luminosities and the results are listed in Table 4. Any difference in the redshift-dependent trends compared to that for the stellar mass relation would indicate changes in the star formation rate per unit stellar mass. Some workers have claimed to see evolution in the M_B-TF relation (Weiner et al. 2006a; Fernández Lorenzo et al. 2010) and we aim to verify or otherwise these trends with our improved data set. As before, we use the local relations of Pierce & Tully (1992) and the $\langle z \rangle \sim 0.3$ study of Bamford et al. (2006) as comparison data sets.

Once again, the intrinsic scatter around our redshift-dependent M_B-TF relations, 0.424, 0.641, 0.670 in mag, at $\langle z \rangle = 0.37, 0.62, 0.96$, are comparable to those seen in the local relations (∼0.4 mag in Pierce & Tully 1992, and 0.3–0.5 in Verheijen 2001), and we note a considerable improvement over previous intermediate-redshift studies. The $\langle z \rangle \sim 0.3$ study of Bamford et al. (2006) and the $\langle z \rangle \sim 0.85$ study of Chiu et al. (2007) have scatters twice as large (∼0.9 in mag), and those of Weiner et al. (2006b) to $z \sim 1.2$ and Fernández Lorenzo et al. (2010) to $z \sim 1.4$ have scatters ≃2–3 times as large (∼1.5 mag and ∼1.2 mag), respectively.

Even though the M_B-TF relation is not as tight as our M_*-TF relation, there is evidence for a stronger evolution in the M_B-TF relation than in the M_*-TF relation, as expected from the well-established increase in disk star formation rate to $z \sim 1$ (Bundy et al. 2005). Fitting a linear regression through the zero points between redshift bins of the enclosed M_B-TF relation we find $\Delta M_B \sim 0.85 \pm 0.28$ mag evolution in the relation from $\langle z \rangle \sim 1.0$ to 0.3. We can check whether this result is affected by a Malmquist bias (given the distribution of luminosities is significantly different between redshift intervals) by comparing subsets with similar luminosities and stellar masses, and the trends do not substantially change. Weiner et al. (2006b) find a consistent trend of ∼1.0–1.5 mag evolution from a similar redshift range of $\langle z \rangle \sim 1.2$ to 0.4, but with more uncertainty. Our results are consistent with the evolution shown in the models of Portinari & Sommer-Larsen (2007): $\Delta M_B \sim 0.85$ from $z \sim 1$. We can understand the different evolutionary trends in the M_B-TF and M_*-TF relations by examining the redshift-dependent correlation between M_B and M_*. To first order, as expected, the difference is explained by the increase in the B-band luminosity per unit stellar mass with redshift (Lilly et al. 1996; Madau et al. 1996).

5. INTERPRETING THE TULLY–FISHER RELATION

We now seek a physical interpretation of the results presented in Section 4 in the context of current models of disk galaxy assembly. First we discuss various procedures for estimating

Table 4
Absolute *B*-band Magnitude Tully–Fisher Relations

z Range	$\langle z \rangle$	N	a[a]	b[b]	$\sigma_{\mathrm{int},V}$[c]	Median σ_V[d]	rms$_V$[e]	$\sigma_{\mathrm{int},M}$[f]	Median σ_M[g]	rms$_M$[h]
Enclosed: $M_B(r_{2.2})$ vs. $V(r_{2.2})$:										
$0.2 < z \leqslant 1.3$	**0.64**	**129**	**−3.589**	**−7.546**	**0.081**	**0.022**	**0.127**	**0.612**	**0.291**	**0.956**
$0.2 < z \leqslant 0.5$	0.37	43	-3.260 ± 0.104	" fixed	0.056	0.035	0.094	0.425	0.245	0.711
$0.5 < z \leqslant 0.8$	0.62	49	-3.703 ± 0.133	" fixed	0.085	0.045	0.130	0.641	0.364	0.979
$0.8 < z \leqslant 1.3$	0.96	37	-3.906 ± 0.162	" fixed	0.089	0.062	0.134	0.670	0.299	1.011
Total: M_B vs. $V(r_D)$										
$0.2 < z \leqslant 1.3$	**0.64**	**129**	**−3.413**	**−7.754**	**0.091**	**0.023**	**0.130**	**0.706**	**0.250**	**1.008**
$0.2 < z \leqslant 0.5$	0.37	43	-3.127 ± 0.114	" fixed	0.065	0.037	0.099	0.505	0.258	0.771
$0.5 < z \leqslant 0.8$	0.62	49	-3.545 ± 0.144	" fixed	0.094	0.057	0.132	0.731	0.364	1.027
$0.8 < z \leqslant 1.3$	0.96	37	-3.624 ± 0.185	" fixed	0.109	0.064	0.144	0.845	0.272	1.114

Notes.
[a] Best-fit y-intercept in mag assuming scatter in $V/\mathrm{km\,s^{-1}}$ dex.
[b] Slope assuming scatter in $V/\mathrm{km\,s^{-1}}$ dex.
[c] Internal scatter in $V/\mathrm{km\,s^{-1}}$ dex.
[d] Median velocity error in $V/\mathrm{km\,s^{-1}}$ dex.
[e] Total scatter in$V/\mathrm{km\,s^{-1}}$ dex.
[f] Internal scatter in mag.
[g] Median B-band magnitude error.
[h] Total scatter in mag.

dynamical masses from our rotation curve data (Section 5.1). We then derive estimates of the total *baryonic mass* (Section 5.3). We combine the two estimates to evaluate the relative roles of baryons and dark matter out to the observable radii probed with our deep exposures (Section 5.4). Although there are considerable uncertainties in what follows, our intent at this stage is to illustrate the possibilities that will arise when gas masses can be determined for samples such as ours so that the total baryonic components would be accurately measured and their role in the TF relation established.

5.1. Dynamical Mass Estimates

The physical basis of our interest in the TF relation is that the dynamical mass is strongly correlated with the luminous and stellar mass components of galaxies, and by analyzing empirical constraints, we can gain an understanding of the relative assembly histories of dark and baryonic matter in galaxies. We thus seek to use our data to estimate both the dynamical masses (i.e., the total mass, including dark and baryonic) as well as that of the stars and gas. Previous studies of this nature (Pizagno et al. 2005; Gnedin et al. 2007; Williams et al. 2010, all low-redshift galaxies) derived dynamical masses from kinematic data that probe sufficiently far in radius to detect the dark halo by revealing a deficit of baryons when dynamic masses are compared to stellar masses.

However, our method of using emission line velocities to estimate the mass within a given radius, such as $r_{2.2}$, depends sensitively on the assumed shape of the underlying gravitational potential, and hence the distribution of mass throughout the disk. For a given ellipsoid potential, the velocity can be most simply approximated as

$$V_c(r)^2 \approx \xi \frac{GM(r)}{r}, \tag{6}$$

where $\xi = 1$ in the case of spherical symmetry. Assuming a *spherical potential* will likely overestimate the disk mass unless a spherical dark matter halo is dominant within the relevant radius. As such it supplies an effective upper limit for a given mass of an ellipsoid calculated from the observed circular velocity. Traditionally, dynamical disk masses have been calculated with an *exponential "Freeman" potential*, solved with modified Bessel functions by assuming a constant mass-to-light ratio and an infinitely thin disk of infinite size (Freeman 1970). This ignores the presence of the bulge and halo, known to be important even at the scales considered here (e.g., Trott et al. 2010; Dutton et al. 2011b). Therefore, as an alternative method of estimating a lower limit, we adopt an *oblate potential*, characterized by a flattening factor q, which is the ratio of the scale length normal to the disk over the scale length of the disk. As shown in Binney & Tremaine (1987), the velocity for an oblate sphere can then be considered as

$$V_c(r)^2 \approx 4\pi G q \int_0^r \frac{\rho(m^2) m^2 dm}{\sqrt{r^2 - m^2(1-q^2)}}, \tag{7}$$

where $m^2 = r^2 + r_s^2$, and ρ is the assumed density function. The exact shape of the potential will depend on the relative contribution of luminous and dark matter, as well as on the triaxial shape of each component. Although halos are believed to be prolate on large scales, their shape is less clear at the scales considered here. Lensing and dynamical studies of individual systems (Dutton et al. 2011b) suggest that they may be considerably rounder. Furthermore, the presence of a bulge generally implies that the stellar distribution is significantly less flat than that of a pure disk. We adopt $q = 0.4$ and an exponential density function as a representative maximum oblateness, equivalent to $\xi \approx 0.752$ for Equation (6). If we were to use a de Vaucouleurs profile (Sérsic profile where $n = 4$) instead of an exponential density profile, ξ would be ≈0.833, resulting in a less than 10% change in the dynamical mass calculation. In the following we will consider the $q = 1$ spherical case and the $q = 0.4$ oblate case as bracketing the shape of the total potential. Additional systematic uncertainties include the effects of non-streaming motions, warps and non-gravitational forces, as discussed in the well-established literature on the interpretation of local rotation curves (see Binney & Tremaine 1987 and references therein). Finally, we consider possible biases arising

from slit spectroscopy and its maximum effect propagated to our dynamical mass estimates in the following section.

5.2. Slit-effect Correction

Recent progress with IFU spectrographs has illustrated some limitations of traditional long-slit and multi-slit techniques in determining the internal dynamics of intermediate-redshift galaxies. This slit-effect is similar to beam smearing in radio astronomy, where the range of velocities from incoming light are averaged over the width of the slit, resulting in a broadening of Doppler shifted lines and an average reduction of the rotational velocity. The magnitude of this effect has been considered in detail by Kapferer et al. (2006) and used by Flores et al. (2006) to compare IFU-derived rotational velocities to those determined with a multi-slit instrument. Kapferer et al. (2006) systematically investigated the effects of various slit widths in combination with inclination, spatial binning and position angle offsets on measured disk velocities using N-body/smoothed particle hydrodynamics simulations. We can use these results to consider the effect our slit geometry might have in distorting our velocities taking into account the galaxy sizes and shapes relative to the DEIMOS slits. Kapferer et al. find no systematic bias due to binning and position angle offset (beyond the correction already made, Section 3.2). We can, however, use Kapferer et al.'s results to calculate an upper-limit approximation of the correction to the velocity $V_{2.2}$ for the effect of the slit width relative to the scale radius (r_s) of each galaxy according to its axis ratio (b/a) and for a given inclination i. Derived from Figures 9 and 10 of Kapferer et al. (2006), the correction is

$$V_{\rm corr} = V_{\rm obs} + V_{\rm beam} \frac{1}{(b/a)} \frac{r_{\rm slit}}{r_s} \sin i, \quad (8)$$

where $V_{\rm beam} \sim 20\,{\rm km\,s^{-1}}$. We find correlations in the correction with respect to scale radius and inclination, but none with mass, redshift, position angle, or observed velocity. The correction added to $V_{2.2}$ ranges from 2 km s^{-1} to 52 km s^{-1}, with a mean of 20 km s^{-1}. These corrections can be found in our catalog.

Because of the imprecise nature of these corrections, arising from the fact that the Kapferer et al. result assumes a symmetric Gaussian to the spectral line profile (while we fit for two half-Gaussians to account for much of the blending between the seeing and dispersion), the Kapferer et al.-based correction remains an upper-limit. Thus we did not include them in our precisely measured TF relations in Section 4. However, we will apply them to our dynamical mass calculation in order to not bias our estimates in a way that may overestimate the dominance of the stellar mass compared to the dark matter. The difference with and without the slit-effect correction can be seen in Figure 10. Because of the imprecision of the analytical formula derived here, we strongly advise against applying such a formula beyond its tested range.

5.3. Baryonic Mass Estimates

In order to examine the redshift-dependent fraction of baryonic mass within $r_{2.2}$ we need to obtain an estimate of the total baryonic mass. In addition to stellar masses, discussed in Section 2.4, we need to account for the presence of gas.

Accurate gas masses are not yet available for intermediate-redshift galaxies, although CO-derived masses have begun to appear for some systems at $z > 1$ with, e.g., the Plateau de Bure Interferometer (Tacconi et al. 2010; Daddi et al. 2010). Nonetheless the situation will improve significantly through upcoming facilities such as the Atacama Large Millimeter/submillimeter Array, the Meer Karoo Array Telescope, and eventually the Square Kilometer Array. Although what follows is somewhat speculative, it provides a reasonable illustration of what will soon be possible. To make progress, we estimated gas masses (M_g) for our sample using the local stellar-to-gas mass (M_*-to-M_g) ratio as a function of M_*, recently parameterized by Peeples & Shankar (2010) based on H I measures from The HI Nearby Galaxy Survey (THINGS) and helium-corrected, CO-derived H_2 masses from the HERA CO-Line EXtragalactic Survey (HERACLES) and the Berkeley–Illinois–Maryland Association Survey of Nearby Galaxies (BIMA SONG) (Leroy et al. 2008).

According to the parameterization by Peeples & Shankar (2010):

$$\frac{M_g}{M_*} = K_f M_*^{-\gamma} \quad (9)$$

where $K_f = 316228$, $\gamma = 0.57$, and M_* is measured in units of solar masses.

Until precision gas masses become available we cannot be certain that the Peeples & Shankar (2010) formalism can be applied in this manner at intermediate redshift. However, locally measured gas-to-stellar mass ratios will underestimate the gas mass for intermediate-redshift galaxies since many stars have subsequently formed. To correct for this, we consider the observed evolution in the specific star formation rate (sSFR) for blue galaxies to $z \sim 2$ as measured by Oliver et al. (2010). To determine the correction for each galaxy, we integrate the best-fit sSFR relation out to the relevant redshift. Oliver et al. (2010) find

$$\mathrm{sSFR} = X(1+z)^{\alpha}, \quad (10)$$

where $\log_{10} X/{\rm Gyr}^{-1} = -1.36 \pm 0.41$ and $\alpha = -3.4 \pm 0.3$. We temper this correction by the gas recycling rate (e.g., Kennicutt et al. 1994; Madau et al. 1998; Cole et al. 2001), estimated to be ~40% for a Chabrier (2003) IMF from $z \sim 1$ to present. This scenario is not strictly a closed-box model, where a galaxy sits in a huge reservoir of gas and simply converts that gas to stars over time. For one, we include the substantial Chabrier recycling rate consistent with the IMF we assume in our stellar mass estimates. The scenario we present here is also consistent with roughly equal inflow and outflow since $z \sim 1$. The fraction of feedback-driven material that exceeds the escape velocity of the galaxy's potential well, and also the typical redshifts at which the filaments that feed galaxies evaporate, are still largely unknown. The gas mass estimates we add to our stellar masses are on average 30% of the total stellar mass estimates, and only exceed that of the stellar mass in a few of the lowest mass objects. So we claim that our gas mass estimates are not the main drivers of our conclusions, and each galaxy's stellar mass and redshift essentially determine the gas mass estimate for this scenario.

5.4. Comparison of Baryonic and Dynamical Masses

We finally turn to our comparison of the dynamical mass with the stellar and baryonic mass. The results of this comparison are given in Figure 10. The top panels show the stellar-to-dynamical mass ratio for a spherical and oblate potential. Across our redshift range we find our stellar-to-dynamical mass fractions are ~0.3 for a spherical potential and ~0.4 for an oblate potential, with considerable scatter. The dynamical

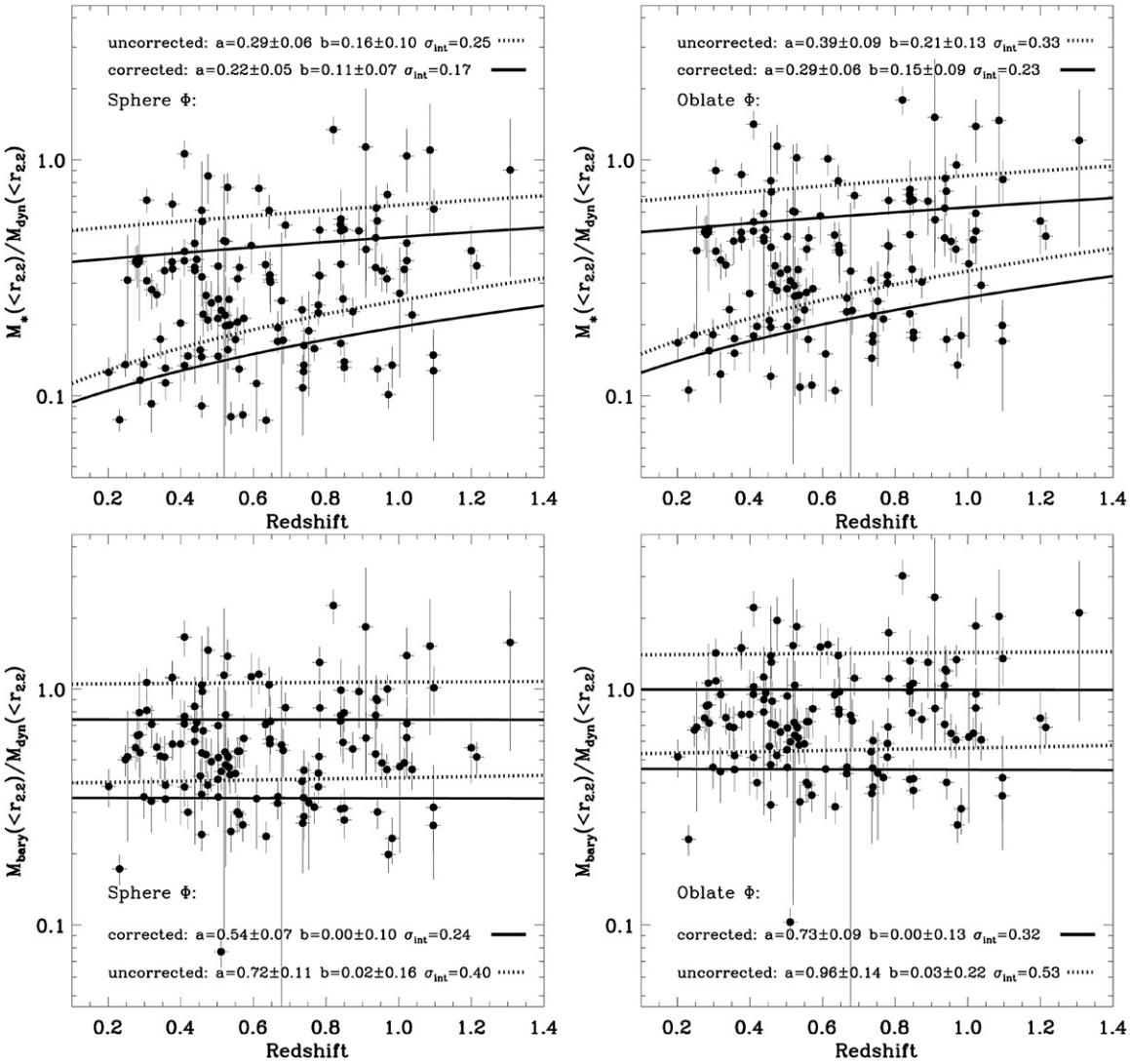

Figure 10. Top panels: stellar-to-dynamical mass ratio within our fiducial $r_{2.2}$ aperture as a function of redshift, assuming a spherical potential (left) and an oblate potential (right). Curves indicate 3σ variations around the best-fit linear relation, with slope b and intercept a. The solid lines are derived from dynamical masses including the slit-effect correction, and the dotted lines are derived from the uncorrected dynamical masses. The scatter around the best-fit relation is also given in each plot. Bottom panels: same as the top panels for baryonic (stellar plus gas) mass.

mass estimates for the points plotted include the slit-effect correction (Section 5.2), representing an upper limit for the dynamical masses, and thus a lower limit for the stellar-to-dynamic mass fraction. For comparison in the plots of Figure 10, the dotted lines are derived from the uncorrected data, and represent a lower limit to the dynamical masses, given an assumed potential shape (spheroid or oblate in our example). The points without slit-effect corrections are not plotted, and only their 3σ best-fit contours are plotted for simplicity. In a few cases, the stellar-to-dynamical fractions are as high as unity, suggesting that baryons play a significant role in driving the TF relation. A dominant baryon fraction is broadly consistent with earlier results by Conselice et al. (2005), Gnedin et al. (2007), Dutton & van den Bosch (2009), and Dutton et al. (2010), especially considering the many uncertainties involved in both mass estimates, including the stellar IMF.

The hypothesis that baryonic mass primarily governs the slow redshift-dependent trends in our observed TF relations is supported further when we attempt to add estimates for the missing gaseous components to our stellar masses. We then find that our baryonic mass estimates within $r_{2.2}$ approach those determined dynamically, with no redshift dependence (bottom panels of Figure 10). The average baryonic-to-dynamical mass ratio is $\sim$50% and $\sim$70%, respectively, for spherical and oblate potentials (including slit-effect corrections). It must be remembered that this baryonic estimate does not include any ionized gas.

Next we explore the radially dependent profile of the dynamical mass as calculated from the rotation curve, to compare it to the baryonic component mass profile. At each tenth of a scale radius along the profile, starting at 1 scale radius, we compute the dynamical mass given the best modeled velocity at that radius in the rotation curve, and compare that to the enclosed baryonic mass at that radius. The baryonic mass is assumed to follow the stellar mass profile, which we approximate to follow the distribution of light found in the reddest *HST* filter ($F850LP$), in an aperture stellar mass estimate, the method of which is described in detail in Section 2.4. The enclosed light at each tenth of a scale radius is compared to the total light, stepping out in elliptical apertures from the photometry, and the aperture mass is calculated from these ratios.

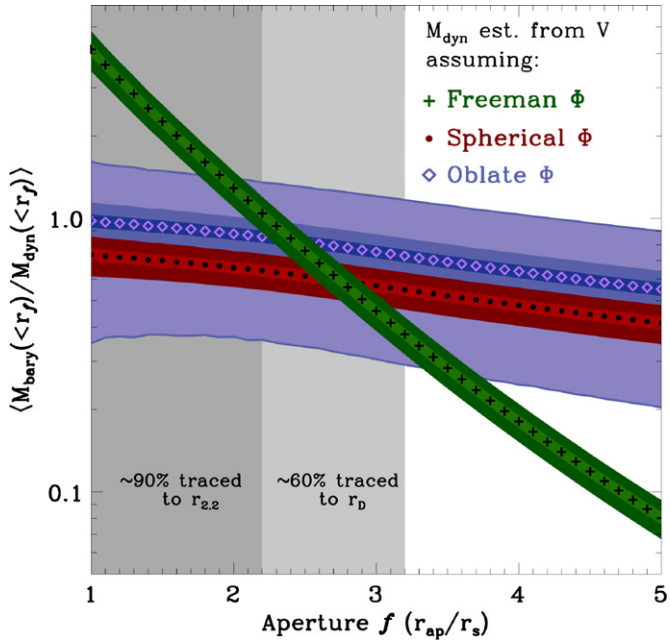

Figure 11. Estimates of the mean baryonic-to-dynamical mass fraction over all redshifts as a function of relative aperture ($f = r/r_s$). Shaded regions show the percentage of disks traced to $f = 2.2$ and 3.2 (r_D); our Keck survey adequately samples the rotational velocities to $f \simeq 3.5$. Different curves relate to different determinations of the dynamic mass (see the text for details) and the tight contours show the one and three times the standard error on the mean. Light shading around the results assuming an oblate potential indicate the aperture-dependent region containing 68% of the individual fractions for our disks. These regions are not shown for the other two potentials, but are of similar size to that of the oblate potential.

Although past studies of rotation curves and the TF relation were often motivated as a means of tracing the influence of dark matter on the baryonic assembly of galaxies, (e.g., Rubin et al. 1980; Vogt et al. 1997; Pizagno et al. 2005; Conselice et al. 2005), it has been suggested in local TF studies that the role of dark matter is minimal in the optical disk (e.g., Courteau & Rix 1999; Palunas & Williams 2000; Bell & de Jong 2001; Kassin et al. 2006). Figure 11 shows that, irrespective of the aperture f, defined in terms of the scale radius (i.e., $f = 2.2$ for $r_{2.2}$), out to the furthest observable extent in our disks, the mean baryonic-to-dynamical fraction is consistent with unity when using an oblate potential for our dynamical mass estimates. In contrast, for a spherical potential, we find that our results permit an equal contribution from dark and baryonic matter by $r_{2.2}$, consistent as we noted above with Portinari & Sommer-Larsen (2007) and Dutton et al. (2011c).

We also show the baryonic-to-dynamical fraction with respect to aperture for a Freeman (1970) potential. The unphysical and sharp rise above unity for small radii shows that the dynamical mass is likely underestimated for the central-most part of the galaxy using this potential. If used in a maximal disk fit, which would re-normalize the sharply rising peak down to unity, the fit would likely result in an underestimate of the overall dynamical contribution of the baryons for what is nominally the scenario where baryons are maximally contributing to the potential. This gives us some indication that the Freeman potential, which assumes a constant mass-to-light ratio for an infinitely thin exponential disk, may not be the best approximation in maximal/minimal fit applications for a disk of a finite thickness and size.

We thus conclude for the scenario presented here that the contribution by baryons to the total mass within the radial range probed by observations is between 50% and 100%. Baryons appear to be the most important component within 2.2 scale radii, and perhaps to larger radii, depending on the uncertain conversion from circular velocity to stellar mass. In addition, such a high fraction of baryons is expected to influence significantly the overall profile of the dark matter halo at these scales through gravitational interactions (see, e.g., Noordermeer et al. 2007 and references therein for a discussion of this topic in the local universe). Therefore even if dark matter is present in an equal amount, it will be tightly coupled to the baryonic content.

6. SUMMARY AND DISCUSSION

Using spectra with extended 6–8 hr integration times secured with the DEIMOS instrument on the Keck II telescope we have measured 129 rotation curves for galaxies selected with $z_{AB} < 22.5$ in the redshift range $0.2 < z < 1.3$ in the two GOODS fields. Using associated *HST* imaging data, we derive modeled velocities corrected for the effects of inclination and seeing to a fiducial radius, $r_{2.2}$, corresponding to 2.2 times the disk scale length. As 90% of our rotation curves flatten within this radius, this gives us a highly reliable set of kinematic data which we use to construct the stellar mass (M_*) and B-band (M_B) TF relations and their evolution over the past 8 Gyr. We find the following results.

1. We demonstrate a significantly reduced scatter around our intermediate-redshift TF relations compared to that seen in earlier studies. The scatter around the M_*-TF relation is typically 0.2 dex of $M_*/M_\odot$, which is two to three times less than earlier work, comparable to that determined locally and less than that achieved by Kassin et al. (2007) who introduced an additional dispersion term in order to achieve a tight relation. The scatter around our M_B-TF relation is typically 0.4–0.7 mag, again comparable to that in local relations and a factor of two to three improvement over earlier work at intermediate redshift. In addition to demonstrating the validity of our observational approach and our improved modeling techniques, our results clearly show the TF relation is well established at redshift $z \simeq 1$.
2. We find a modest but statistically insignificant evolution in the M_*-TF relation with redshift corresponding to a growth in stellar mass at fixed velocity of $\Delta M_* = 0.04 \pm 0.07$ dex with cosmic time from a redshift $\langle z \rangle \simeq 1.0$ to 0.3. This is consistent with the results of recent numerical and semi-analytic simulations (Portinari & Sommer-Larsen 2007; Somerville et al. 2008; Dutton et al. 2011a).
3. More pronounced evolution is seen in the M_B-TF relation corresponding to a decline in luminosity of 0.85 ± 0.28 mag from $\langle z \rangle \simeq 1.0$ to 0.3, again consistent with predictions from Portinari & Sommer-Larsen (2007). The origin of this evolution can be understood by examining the mass-dependent correlation between M_* and M_B as a function of redshift. Together with the larger scatter seen in the M_B-TF relation than in that based on stellar mass, this demonstrates that the M_*-TF relation is the more fundamental descriptor of disk galaxy assembly.
4. We finally use our data to illustrate the potential of comparing dynamical and baryonic masses to better understand the contributions that they matter make in the M_*-TF relation. Although we are uniquely placed to explore our extended

rotation curves and carefully derived stellar masses, our gas mass estimates are clearly approximate at this stage. We estimate dynamical masses using both spherical and oblate potentials which we expect bracket the likely values. We compute baryonic masses by estimating the additional mass in cold gas. We find that baryons may contribute between 50% and 100% of the total mass within the radii at which we can confidently observe dynamics of the gas in our disk sample. Such a high fraction of baryons influence significantly the overall profile of the dark matter halo. Even if dark matter is present in an equal amount, it will be tightly coupled to the baryonic content.

S.H.M. thanks the Rhodes Trust, the Oxford Astrophysics Department, New College, Oxford, and the California Institute of Technology for supporting her work. M.S. and R.S.E. acknowledge financial support from the Royal Society. We thank S. Moran, N. Miller, G. Mikelsons, and K. Chiu for considerable initial assistance with the organization of this data set. We thank C. Peng for supplying us with GALFIT 3.0 and acknowledge useful discussions with A. Benson, A. Brooks, A. Bunker, M. Bureau, M. Cappellari, R. Davies, H. Flores, F. Hammer, S. Kassin, L. Miller, and M. Puech. The referee, B. Weiner, is acknowledged for his constructive comments in the improvement of this paper. The spectroscopic data was secured with the W. M. Keck Observatory on Mauna Kea. We thank the observatory staff for their dedication and support. The authors recognize and acknowledge the cultural role and reverence that the summit of Mauna Kea has always had with the indigenous Hawaiian community. We are most fortunate to have the opportunity to conduct observations from this mountain.

REFERENCES

Atkinson, N., Conselice, C. J., & Fox, N. 2007, arXiv:0712.1316
Bamford, S. P., Aragón-Salamanca, A., & Milvang-Jensen, B. 2006, MNRAS, 366, 308
Bell, E. F., & de Jong, R. S. 2001, ApJ, 550, 212
Benson, A. J., Bower, R. G., Frenk, C. S., et al. 2003, ApJ, 599, 38
Binney, J., & Tremaine, S. 1987, Galactic Dynamics (Princeton, NJ: Princeton Univ. Press)
Blumenthal, G. R., Faber, S. M., Flores, R., & Primack, J. R. 1986, ApJ, 301, 27
Böhm, A., & Ziegler, B. L. 2007, in ASP Conf. Ser. 379, Cosmic Frontiers, ed. N. Metcalfe & T. Shanks (San Francisco, CA: ASP), 278
Böhm, A., Ziegler, B. L., Saglia, R. P., et al. 2004, A&A, 420, 97
Brinchmann, J., & Ellis, R. S. 2000, ApJ, 536, L77
Bruzual, G., & Charlot, S. 2003, MNRAS, 344, 1000
Bundy, K., Ellis, R. S., & Conselice, C. J. 2005, ApJ, 625, 621
Bundy, K., Fukugita, M., Ellis, R. S., et al. 2009, ApJ, 697, 1369
Chabrier, G. 2003, PASP, 115, 763
Chiu, K., Bamford, S. P., & Bunker, A. 2007, MNRAS, 377, 806
Coil, A. L., Davis, M., Madgwick, D. S., et al. 2004, ApJ, 609, 525
Cole, S., Norberg, P., Baugh, C. M., et al. 2001, MNRAS, 326, 255
Conselice, C. J., Bundy, K., Ellis, R. S., et al. 2005, ApJ, 628, 160
Courteau, S. 1996, ApJS, 103, 363
Courteau, S. 1997, AJ, 114, 2402
Courteau, S., & Rix, H. 1997, BAAS, 29, 1332
Courteau, S., & Rix, H.-W. 1999, ApJ, 513, 561
Cresci, G., Hicks, E. K. S., Genzel, R., et al. 2009, ApJ, 697, 115
Daddi, E., Bournaud, F., Walter, F., et al. 2010, ApJ, 713, 686
Dalcanton, J. J., Spergel, D. N., & Summers, F. J. 1997, ApJ, 482, 659
Davis, M., Faber, S. M., Newman, J., et al. 2003, Proc. SPIE, 4834, 161
Dickinson, M., Giavalisco, M., & GOODS Team. 2003, in The Mass of Galaxies at Low and High Redshift, ed. R. Bender & A. Renzini (Berlin: Springer), 324
Dutton, A. A., Bosch, F. C. V. D., Faber, S. M., et al. 2011a, MNRAS, 410, 1660
Dutton, A. A., Brewer, B. J., Marshall, P. J., et al. 2011b, arXiv:1101.1622
Dutton, A. A., Conroy, C., van den Bosch, F. C., Prada, F., & More, S. 2010, MNRAS, 407, 2
Dutton, A. A., Conroy, C., van den Bosch, F. C., et al. 2011c, MNRAS, 416, 322
Dutton, A. A., & van den Bosch, F. C. 2009, MNRAS, 396, 141
Dutton, A. A., van den Bosch, F. C., Dekel, A., & Courteau, S. 2007, ApJ, 654, 27
Eke, V. R., Navarro, J. F., & Steinmetz, M. 2001, ApJ, 554, 114
Ellis, R., & Silk, J. 2009, New Frontiers in Cosmology and Galaxy Formation: Challenges for the Future (Cambridge: Cambridge Univ. Press), 133
Faber, S. M., Phillips, A. C., Kibrick, R. I., et al. 2003, Proc. SPIE, 4841, 1657
Faber, S. M., Willmer, C. N. A., Wolf, C., et al. 2007, ApJ, 665, 265
Fall, S. M., & Efstathiou, G. 1980, MNRAS, 193, 189
Fernández Lorenzo, M., Cepa, J., Bongiovanni, A., et al. 2009, A&A, 496, 389
Fernández Lorenzo, M., Cepa, J., Bongiovanni, A., et al. 2010, A&A, 521, A27
Flores, H., Hammer, F., Puech, M., Amram, P., & Balkowski, C. 2006, A&A, 455, 107
Förster Schreiber, N. M., Genzel, R., Bouché, N., et al. 2009, ApJ, 706, 1364
Freeman, K. C. 1970, ApJ, 160, 811
Genzel, R., Tacconi, L. J., Eisenhauer, F., et al. 2006, Nature, 442, 786
Giavalisco, M., Ferguson, H. C., Koekemoer, A. M., et al. 2004, ApJ, 600, L93
Gnedin, O. Y., Weinberg, D. H., Pizagno, J., Prada, F., & Rix, H. 2007, ApJ, 671, 1115
Gnerucci, A., Marconi, A., Cresci, G., et al. 2011, A&A, 528, 88
Governato, F., Willman, B., Mayer, L., et al. 2007, MNRAS, 374, 1479
Haynes, M. P., & Giovanelli, R. 1984, AJ, 89, 758
Jones, T., Ellis, R., Jullo, E., & Richard, J. 2010, ApJ, 725, L176
Kapferer, W., Ferrari, C., Domainko, W., et al. 2006, A&A, 447, 827
Kassin, S. A., de Jong, R. S., & Weiner, B. J. 2006, ApJ, 643, 804
Kassin, S. A., Weiner, B. J., Faber, S. M., Koo, D. C., & Lotz, J. M. 2007, in ASP Conf. Ser. 380, Deepest Astronomical Surveys, ed. J. Afonso, H. C. Ferguson, B. Mobasher, & R. Norris (San Francisco, CA: ASP), 477
Kelly, B. C. 2007, ApJ, 665, 1489
Kennicutt, R. C., Jr., Tamblyn, P., & Congdon, C. E. 1994, ApJ, 435, 22
Le Fèvre, O., Vettolani, G., Paltani, S., et al. 2004, A&A, 428, 1043
Leroy, A. K., Walter, F., Brinks, E., et al. 2008, AJ, 136, 2782
Lilly, S. J., Le Fevre, O., Hammer, F., & Crampton, D. 1996, ApJ, 460, L1
Madau, P., Ferguson, H. C., Dickinson, M. E., et al. 1996, MNRAS, 283, 1388
Madau, P., Pozzetti, L., & Dickinson, M. 1998, ApJ, 498, 106
Markwardt, C. B. 2009, in ASP Conf. Ser. 411, ed. D. A. Bohlender, D. Durand, & P. Dowler (San Francisco, CA: ASP), 251
Meyer, M. J., Zwaan, M. A., Webster, R. L., Schneider, S., & Staveley-Smith, L. 2008, MNRAS, 391, 1712
Mo, H. J., & Mao, S. 2000, MNRAS, 318, 163
Mo, H. J., Mao, S., & White, S. D. M. 1998, MNRAS, 295, 319
Moran, S. M., Miller, N., Treu, T., Ellis, R. S., & Smith, G. P. 2007, ApJ, 659, 1138
Noordermeer, E., van der Hulst, J. M., Sancisi, R., Swaters, R. S., & van Albada, T. S. 2007, MNRAS, 376, 1513
Oliver, S., Frost, M., Farrah, D., et al. 2010, MNRAS, 405, 2279
Palunas, P., & Williams, T. B. 2000, AJ, 120, 2884
Peeples, M. S., & Shankar, F. 2010, arXiv:1007.3743
Peng, C. 2010, BAAS, 42, 578
Persic, M., Salucci, P., & Stel, F. 1996, MNRAS, 281, 27
Pierce, M. J., & Tully, R. B. 1992, ApJ, 387, 47
Piontek, F., & Steinmetz, M. 2011, MNRAS, 410, 2625
Pizagno, J., Prada, F., Weinberg, D. H., et al. 2005, ApJ, 633, 844
Portinari, L., & Sommer-Larsen, J. 2007, MNRAS, 375, 913
Puech, M., Flores, H., Hammer, F., et al. 2008, A&A, 484, 173
Retzlaff, J., Rosati, P., Dickinson, M., et al. 2010, A&A, 511, A50
Rix, H., Guhathakurta, P., Colless, M., & Ing, K. 1997, MNRAS, 285, 779
Rubin, V. C., Ford, W. K. J., & Thonnard, N. 1980, ApJ, 238, 471
Seljak, U., Makarov, A., McDonald, P., et al. 2005, Phys. Rev. D, 71, 103515
Shapiro, K. L., Genzel, R., Förster Schreiber, N. M., et al. 2008, ApJ, 682, 231
Shlosman, I. 2009, in ASP Conf. Ser. 419, ed. S. Jogee, I. Marinova, L. Hao, & G. A. Blanc (San Francisco, CA: ASP), 39
Somerville, R. S., Barden, M., Rix, H., et al. 2008, ApJ, 672, 776
Spergel, D. N., Bean, R., Doré, O., et al. 2007, ApJS, 170, 377
Stark, D. P., Swinbank, A. M., Ellis, R. S., et al. 2008, Nature, 455, 775
Steinmetz, M., & Navarro, J. F. 1999, ApJ, 513, 555
Tacconi, L. J., Genzel, R., Neri, R., et al. 2010, Nature, 463, 781
Trott, C. M., Treu, T., Koopmans, L. V. E., & Webster, R. L. 2010, MNRAS, 401, 1540
Tully, R. B., & Fisher, J. R. 1977, A&A, 54, 661
Tully, R. B., Pierce, M. J., Huang, J., et al. 1998, AJ, 115, 2264
van den Bosch, F. C. 2000, ApJ, 530, 177
Verheijen, M. A. W. 2001, ApJ, 563, 694

Vogt, N. P., Forbes, D. A., Phillips, A. C., et al. 1996, ApJ, 465, L15
Vogt, N. P., Phillips, A. C., Faber, S. M., et al. 1997, ApJ, 479, L121
Wechsler, R. H., Bullock, J. S., Primack, J. R., Kravtsov, A. V., & Dekel, A. 2002, ApJ, 568, 52
Weiner, B. J., Willmer, C. N. A., Faber, S. M., et al. 2006a, ApJ, 653, 1049
Weiner, B. J., Willmer, C. N. A., Faber, S. M., et al. 2006b, ApJ, 653, 1027
Williams, M. J., Bureau, M., & Cappellari, M. 2010, MNRAS, 409, 1330
Willick, J. A. 1999, ApJ, 516, 47
Wirth, G. D., Willmer, C. N. A., Amico, P., et al. 2004, AJ, 127, 3121
Wolf, C., Meisenheimer, K., Kleinheinrich, M., et al. 2004, A&A, 421, 913
Ziegler, B. L., Böhm, A., Fricke, K. J., et al. 2002, ApJ, 564, L69